Substantial Warming of the Atlantic Ocean in CMIP6 Models

QIUPING REN,[a] YOUNG-OH KWON,[c] JIAYAN YANG,[c] RUI XIN HUANG,[c] YUANLONG LI,[a,b] AND FAN WANG[a,b]

[a] *CAS Key Laboratory of Ocean Circulation and Waves, Institute of Oceanology, Chinese Academy of Sciences, Qingdao, China*
[b] *Laoshan Laboratory, Qingdao, China*
[c] *Woods Hole Oceanographic Institution, Woods Hole, Massachusetts*

(Manuscript received 14 July 2023, in final form 7 December 2023, accepted 22 February 2024)

ABSTRACT: The storage of anthropogenic heat in oceans is geographically inhomogeneous, leading to differential warming rates among major ocean basins with notable regional climate impacts. Our analyses of observation-based datasets show that the average warming rate of 0–2000-m Atlantic Ocean since 1960 is nearly threefold stronger than that of the Indo-Pacific Oceans. This feature is robustly captured by historical simulations of phase 6 of Coupled Model Intercomparison Project (CMIP6) and is projected to persist into the future. In CMIP6 simulations, the ocean heat uptake through surface heat fluxes plays a central role in shaping the interbasin warming contrasts. In addition to the slowdown of the Atlantic meridional overturning circulation as stressed in some existing studies, alterations of atmospheric conditions under greenhouse warming are also essential for the increased surface heat flux into the North Atlantic. Specifically, the reduced anthropogenic aerosol concentration in the North Atlantic since the 1980s has been favorable for the enhanced Atlantic Ocean heat uptake in CMIP6 models. Another previously overlooked factor is the geographic shape of the Atlantic Ocean which is relatively wide in midlatitudes and narrow in low latitudes, in contrast to that of the Indo-Pacific Oceans. Combined with the poleward migration of atmospheric circulations, which leads to the meridional pattern of surface heat uptake with broadly enhanced heat uptake in midlatitude oceans due to reduced surface wind speed and cloud cover, the geographic shape effect renders a higher basin-average heat uptake in the Atlantic.

KEYWORDS: Climate change; Climate models; Atlantic Ocean; Atmospheric circulation; Heat budgets/fluxes; Temperature

1. Introduction

The ocean has stored more than 90% of the excessive heat of Earth induced by the increasing atmospheric greenhouse gas concentration and showed pervasive warming in most parts (e.g., Trenberth et al. 2009; Johnson et al. 2021; Cheng et al. 2022). The ocean heat storage (change of ocean heat content) is, however, geographically nonuniform, and the Atlantic Ocean has shown enhanced heat storage (e.g., Johnson and Lyman 2020; Levitus et al. 2012; Shi et al. 2018; Lee et al. 2011) and a higher average warming pace in the 0–2000-m layer than the Indo-Pacific Oceans (Fig. 1). According to Cheng et al. (2022), the Atlantic Ocean between 35°S and 64°N has contributed about 33% to the 0–2000-m global ocean heat content increase during 1958–2019.

The substantial warming of the Atlantic Ocean has widespread impacts, both regionally and globally, on sea level rise in low-lying coasts and islands (Sallenger et al. 2012; Frederikse et al. 2020), increased occurrence of marine heatwaves (Wernberg et al. 2016; Frölicher et al. 2018) and hurricanes (Balaguru et al. 2023), enhancement of upper-ocean stratification (Li et al. 2020), decline in marine primary productivity (Boyce et al. 2010), and far-reaching impacts on tropical climates of the Indo-Pacific Oceans (Li et al. 2016; Cai et al. 2019). Most importantly, the warming of the high-latitude North Atlantic Ocean accelerates the Arctic sea ice melting (e.g., Trenberth and Fasullo 2017; Zhang 2015) and the retreat of Greenland's outlet glaciers (e.g., Straneo and Heimbach 2013), which lead to a slowdown of the Atlantic meridional overturning circulation (AMOC) (e.g., Ferster et al. 2022; McCarthy and Thorne 2018; Rahmstorf et al. 2015; Caesar et al. 2018; Boers 2021). Enhanced heat storage in the Atlantic Ocean also modulates the pace of global surface warming (e.g., Chen and Tung 2014, 2018) and transient climate responses to anthropogenic radiative forcing—the climate sensitivity (e.g., Rose et al. 2014; Marshall et al. 2015; Romanou et al. 2017). With these considerations, mechanistic understandings of the substantial Atlantic Ocean warming are of scientific significance and practical priority.

Regional ocean heat storage is determined by the balance between surface heat uptake through surface heat fluxes and heat convergence induced by oceanic circulation and mixing (e.g., Banks and Gregory 2006; Bronselaer and Zanna 2020; Armour et al. 2016; Dias et al. 2020). These two processes are often not independent of each other. Weakening of the AMOC, while driving lateral heat flux convergence in the tropical–subtropical Atlantic (Grist et al. 2010; McMonigal et al. 2023; Palmer and Haines 2009; Gregory et al. 2016), exerts a "redistribution feedback" onto surface heat flux (Hu et al. 2020) and enhances surface heat uptake in the subpolar North Atlantic (Xie and Vallis 2012; Dias et al. 2020; Garuba and Klinger 2018, 2016; Gregory et al. 2016). Xie and Vallis (2012) demonstrated a slowdown of the AMOC may give rise to the North Atlantic warming hole (NAWH)—a subpolar region showing surface cooling or reduced warming (e.g., Liu et al. 2020; Chemke et al. 2020; Hu and Fedorov 2020; He et al. 2022)—and thereby suppresses

Supplemental information related to this paper is available at the Journals Online website: https://doi.org/10.1175/JCLI-D-23-0418.s1.

Corresponding authors: Qiuping Ren, renqiuping@qdio.ac.cn; Yuanlong Li, liyuanlong@qdio.ac.cn

DOI: 10.1175/JCLI-D-23-0418.1

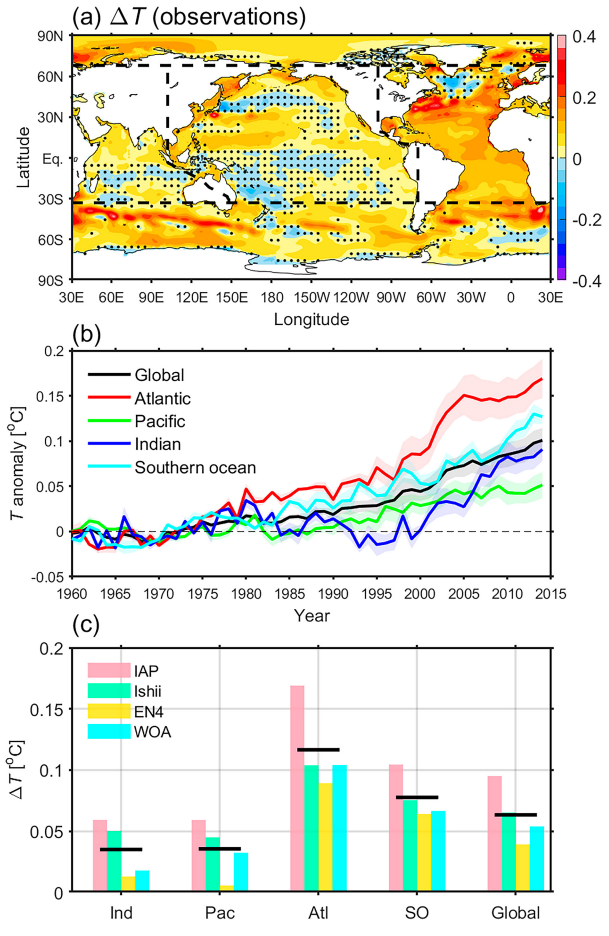

FIG. 1. (a) The 0–2000-m averaged ocean temperature changes (ΔT; °C) derived from the observational dataset ensemble mean. The ΔT is calculated as the temperature difference between the 1994–2014 and 1960–80 periods. The dashed lines mark the boundaries between ocean basins. Stippling indicates insignificant ΔT values at the 95% confidence level based on the Student's t test. (b) The 0–2000-m averaged ocean temperatures for the global ocean and individual ocean basins are derived from the observational datasets, shown as anomalies relative to the 1960–80 baseline. Thick curves and shadings denote the ensemble mean and one standard error range of datasets, respectively. (c) The averaged ΔT for the global ocean and individual ocean basins, i.e., Indian Ocean (Ind), Pacific Ocean (Pac), Atlantic Ocean (Atl), and Southern Ocean (SO) from four observational datasets, respectively, with the black lines showing the ensemble mean of four datasets.

upward turbulent heat release toward the atmosphere. The redistribution feedback of the AMOC explained a large portion of the Atlantic heat content increase in the CO_2 quadrupling model experiment by Garuba and Klinger (2016). Meanwhile, warming in the tropical and subtropical Atlantic has been attributed to the interplay between increased stratification and equatorward heat transport by the subtropical gyres (Dias et al. 2020; Grist et al. 2010; Palmer and Haines 2009). Existing studies have also shown that the changes in the wind-driven gyre circulation play essential roles in shaping the heat storage pattern (Garuba and Klinger 2018; He et al. 2022; McMonigal et al. 2023; Duan et al. 2023). Lee et al. (2011) put forward that the strengthened Agulhas leakage transport in response to the poleward migration of westerly winds in the Southern Ocean (Backeberg et al. 2012) has contributed to the substantial Atlantic Ocean warming since the mid-twentieth century.

While studies based on model simulations have largely stressed the essential role of ocean circulation, particularly the AMOC, the long-term changes of the Atlantic Ocean circulation are subjected to considerable uncertainties (e.g., Fu et al. 2020; Worthington et al. 2021; Parker and Ollier 2021). For example, the IPCC-class climate models contain long-standing biases in simulating overturning circulations (Wang et al. 2014) and are incapable of properly resolving the eddy-driven Agulhas leakage transport (Beal et al. 2015; Zhang et al. 2023a,b). While instrument-based observations are insufficient for robustly isolating the long-term trends of the Atlantic Ocean circulation from natural variability, reconstructions and proxies exhibit a widespread in the AMOC changes ranging from dramatic to no weakening in the last several decades (Fu et al. 2020; Worthington et al. 2021; Parker and Ollier 2021; Rahmstorf et al. 2015). Changes of the Agulhas Current in the past few decades also remain uncertain (Zhang et al. 2023b; Beal et al. 2011). Therefore, to better understand the Atlantic Ocean warming in observations and model simulations, other possible drivers are worthy of further investigation, complementary to the well-recognized role of ocean circulations.

Actually, atmospheric processes also modulate air–sea heat fluxes (Lyu et al. 2020; Hu et al. 2020; Garuba and Klinger 2018). Changes in atmospheric conditions, broadly including winds, air temperature and humidity, cloud cover, and aerosol concentrations can perturb heat fluxes into the ocean and affect ocean heat uptake. Dramatic changes have been observed in atmospheric circulations in the past decades, with the poleward shift of westerly winds and poleward expansion of the Hadley circulation being salient features (Yang et al. 2020, 2022; Gonzalez et al. 2019; Hu et al. 2013, 2018; Mitas and Clement 2005; Grise et al. 2019; Pikovnik et al. 2022). The changes in atmospheric circulation also involve notable changes in regional cloud cover and radiation feedback (Park et al. 2006; Clement et al. 2009). In addition, the spatially heterogeneous, time-varying aerosol emissions, featured an increase in Asia and a decline in North America and Europe during the past decades (Y. Wang et al. 2015; Shi et al. 2022), may also have altered the heat storage pattern (Myhre et al. 2013; von Schuckmann et al. 2016; Giannini and Kaplan 2019; Hirasawa et al. 2020). Whether and how these significant atmospheric changes may affect the accelerated Atlantic Ocean warming remain to be clarified.

Mechanistic understanding of the Atlantic Ocean warming in observations and model simulations is pursued in the present study by analyzing phase 6 of the Coupled Model Intercomparison Project (CMIP6) simulations (Eyring et al. 2016) and existing gridded observational temperature datasets. The remainder of the paper is organized as follows. In section 2, we introduce observation-based datasets and CMIP6 models, as well as methods used in our study. In section 3, we describe the observed and simulated substantial Atlantic Ocean warming, track the heat source in CMIP6, and expound the atmosphere-forcing mechanisms underlying the substantial Atlantic Ocean warming by

assessing the changes in surface heat fluxes and atmospheric conditions. In section 4, we provide a summary and discussion of our findings.

2. Data and methods

a. Observation-based datasets

We analyzed four global observational datasets of ocean temperature with 1° × 1° horizontal resolution: the Institute of Atmospheric Physics (IAP) ocean objective monthly analysis provided by the Chinese Academy of Sciences (Cheng et al. 2017), the monthly Ishii V7.2 data provided by the Japan Marine Science and Technology Center (Ishii et al. 2017), the monthly EN4.2.0 from the Met Office (Good et al. 2013), and the pentad mean *World Ocean Atlas* (*WOA*) from the U.S. National Centers for Environmental Information (Levitus et al. 2012). In this study, we utilize the temperature fields in 0–2000 m from these datasets for the period of 1960–2014. The ending year of 2014 is chosen to match the historical simulations of CMIP6.

Although many efforts have been made to improve estimates of historical temperature change (e.g., Cheng et al. 2017; Ishii et al. 2017; Good et al. 2013; Levitus et al. 2012), an accurate assessment is still a challenge due to insufficient and irregular data coverage mainly during the pre-Argo era (Lyman and Johnson 2014; Durack et al. 2014; Cheng and Zhu 2014; Good 2016). In our analysis, the ensemble average of the four datasets is referred to as "observations" and its uncertainty is quantified by ±1 standard error across the datasets. Note that all datasets substantially use the same sampling data, and the same sampling or instrument bias errors may be retained in the datasets, so that their standard error may underestimate the uncertainties.

b. CMIP6

We analyzed monthly data from 24 CMIP6 historical simulations for 1960–2014, which are forced with the observed well-mixed greenhouse gases, aerosols, and stratospheric ozone depletion (Eyring et al. 2016). In addition, we analyzed projection simulations under the Shared Socioeconomic Pathways (SSP) 1-2.6, SSP2-4.5, and SSP5-8.5 for 2015–2100 from 15 different models (O'Neill et al. 2016). The analyzed variables include three-dimensional ocean potential temperature and two-dimensional fields of the surface heat fluxes, sea surface temperature (SST), surface air temperature, air specific humidity at the sea surface and 10 m above the surface, near-surface winds at 10 m, cloud cover, precipitation rate, geopotential height (GPH), total aerosol concentration, and the northward heat flux in the Atlantic Ocean. The net surface heat flux is from the ocean model, which accounts for both the air–sea flux and ice–sea flux, thus the total heat flux into the ocean from the surface (Shu et al. 2022). In addition, the following components are also examined: shortwave radiation (SWR), longwave radiation (LWR), turbulent heat flux (THF) including sensible heat flux (SHF) and latent heat flux (LHF), and heat flux into seawater due to frazil ice formation Q_{ice}. The frazil ice is a kind of fine crystals that are formed in supercooled seawater (Matsumura and Ohshima 2015). The heat flux due to underwater frazil ice formation also influences the ocean heat uptake in the polar regions (Graham and Vellinga 2013). The models and variables used in this study are specified in Table 1.

The CMIP6 models provide large ensemble members that have different variant labels based on realizations (r), initialization (i) schemes, different physics (p), and forcing (f) indices. The first realization members (r1i1p1f1) of models for both historical and SSP scenarios are chosen in our analysis—a widely adopted choice of existing studies. CMIP6 models used in this study contain a wide range of spatial resolutions and different map projections (Table 1 in the online supplemental material). Generally, the finer resolution models produce a better performance of surface heat flux simulations (Lin and Yu 2022). For comparison, we interpolated all model outputs onto regular 1° × 1° grids for our analysis. The multimodel mean (MMM) of CMIP6 models reduces biases and extracts the effect of external forcing. The intermodel spread is quantified by the ±1 standard error range of models, representing the amplitude of internal climate variability and model structural differences.

c. Statistical calculations

For all the observation-based and model data, the long-term change Δ during 1960–2014 is estimated as the differences between the averages in 1960–80 and 1994–2014. The observed changes are subjected to poor data samplings during 1960–80, which leads to uncertainties in the estimated warming rates. In future warming scenarios of CMIP6, the projected changes are estimated as the differences between the 2080–2100 and 2015–35 periods. The statistical significance of the change is estimated based on the two-tailed Student's *t* test.

Besides, the basin-average temperature change is computed as follows:

$$\Delta T_{\text{basin}} = \frac{\int \Delta T dA}{\int dA}, \tag{1}$$

where dA is the area of each grid point and $\int dA$ is the total area of individual oceans.

d. Surface heat uptake calculation

To link regional heat storage to surface uptake, we analyze the heat budget within the upper 2000-m ocean. The 0–2000-m average ocean temperature tendency $\partial T/\partial t$ can be separated into two terms: the surface heat uptake and residual:

$$\frac{\partial T}{\partial t} = \frac{Q_{\text{net}}}{\rho C_p H} + R, \tag{2}$$

where Q_{net} is the net surface heat flux (positive being into the ocean either from the atmosphere or sea ice) as the sum of the air–sea surface heat fluxes as explained above and ice–sea heat flux associated with melting/freezing from the ocean model component, $\rho = 1024\ \text{kg m}^{-3}$ is the seawater density, $c_p = 3996\ \text{J K}^{-1}\ \text{kg}^{-1}$ is the specific heat capacity of seawater, and $H = 2000$ m is the depth range covered by observational datasets (in areas shallower than 2000 m, the bottom depth is adopted for H). Note that the surface heat uptake in ice-covered areas should be calculated using the ice–sea heat fluxes rather than air–sea fluxes so that we use the Q_{net} data from ocean model outputs (see Table 1). The R is

TABLE 1. Variables and models used in this study from CMIP6 historical simulations and projection simulations under the SSP1-2.6, SSP2-4.5, and SSP5-8.5. Omon and Amon stand for the monthly outputs from the ocean and atmospheric model components, respectively. Note that the 11 CMIP6 historical simulations (bold font) also provide the Omon SWR, LWR, and THF.

Variables	Models			
		Historical		
Potential temperature (Omon) Surface net heat flux (Omon)	**ACCESS-CM2**	NorESM2-LM	**CAMS-CSM1-0**	MPI-ESM1-2-HR
SWR and LWR (Amon) LHF and SHF (Amon)	**CESM2**	**CESM2-FV2**	**CESM2-WACCM**	**CESM2-WACCM-FV2**
Air specific humidity (Amon) SST (Omon)	MIR0C6	**CMCC-ESM2**	**FIO-ESM-2-0**	MPI-EMS-1-2-HAM
Surface air temperature (Amon) WS (Amon)	CanESM5	GISS-E2-1-G	GISS-E2-1-H	**CMCC-CM2-SR5**
Near-surface zonal wind (Amon) Cloud cover (Amon)	FGOALS-g3	CAS-ESM2-0	MPI-ESM1-2-LR	**MRI-ESM2-0**
Precipitation (Amon) GPH (Amon)	TaiESM1	NorESM2-MM	SAM0-UNICON	**ACCESS-ESM1-5**
Aerosol concentration (Amon)	CESM2 MRI-ESM2-0	CESM2-FV2	CESM2-WACCM	CESM2-WACCM-FV2
Meridional heat flux (Omon)	CanESM5 FGOALS-g3 CIESM EC-Earth3	CMCC-CM2-SR5 GISS-E2-1-G SAM0-UNICON CMCC-ESM2	EC-Earth3-CC MPI-ESM1-2-HR EC-Earth3-Veg	MPI-ESM1-2-LR MPI-ESM-1-2-HAM EC-Earth3-Veg-LR
Heat flux into sea water due to frazil ice formation (Omon)	ACCESS-CM2 CESM2-FV2 MIROC6	CESM2-WACCM CMCC-ESM2 FIO-ESM-2-0	MRI-ESM2-0 CMCC-CM2-SR5	ACCESS-ESM1-5 CESM2-WACCM-FV2
		Projections		
Potential temperature (Omon)	ACCESS-CM2 NESM3	MIROC6 FGOALS-g3	CanESM5 CAM-CSM1-0	CESM2-WACCM EC-Earth3-Veg
Net surface heat flux (Omon)	CIESM EC-Earth3	GFDL-CM4 GFDL-ESM4	FIO-ESM-2-0 MRI-ESM2-0	MPI-ESM1-2-LR

the residual term, including the heat flux convergence by ocean dynamics (advection, mixing, and diffusion) and calculation errors. The temperature anomaly induced by surface heat uptake T'_{uptake} is calculated by integrating surface net heat flux anomaly Q'_{net} over time:

$$T'_{\text{uptake}}(t) = \int_{1960}^{t} \frac{Q'_{\text{net}}(t)}{\rho C_p H} dt, \tag{3}$$

where Q'_{net} is the anomaly relative to the 1960–80 baseline. The temperature change driven by surface heat uptake ΔT_{uptake} is computed as the difference between averaged T'_{uptake} in 1960–80 and 1994–2014, respectively. The residual temperature change ΔT_{res} is computed simply as the difference between the total change ΔT and ΔT_{uptake}:

$$\Delta T_{\text{res}} = \Delta T - \Delta T_{\text{uptake}}. \tag{4}$$

The comparison between ΔT_{uptake} and ΔT_{res} is different from the comparison between the added heat and redistributed heat in some studies (e.g., Cheng et al. 2022; Xie and Vallis 2012; Dias et al. 2020; Garuba and Klinger 2018, 2016; Gregory et al. 2016) because ΔT_{uptake} induced by net surface heat flux changes is confounded by the effects of atmospheric forcing and oceanic redistribution feedbacks (Hu and Fedorov 2020).

3. Results

a. Warming of the 0–2000-m Atlantic Ocean

We first assess the long-term change of the 0–2000-m average temperature ΔT for 1960–2014 from available observations and CMIP6 models. Observational datasets reveal a geographically inhomogeneous ΔT pattern over the global ocean, with significant warming in some regions and insignificantly weak warming or even cooling trends in others at the 95% confidence level (Fig. 1a). Except for the NAWH region between 45° and 60°N, the Atlantic Ocean shows significant warming trends at the 95% confidence level that are much stronger than those in the Indo-Pacific Oceans. The maximum ΔT of ~0.36°C is located along the Gulf Stream in observations. In terms of the basin-average ΔT, the Atlantic Ocean has been warming up at a higher rate than the other oceans, particularly since the 1980s (Fig. 1b; Cheng et al. 2022, 2017). The

substantial warming of the Atlantic Ocean is the common feature of the four observational datasets (Fig. 1c). The basin-average ΔT of the Atlantic Ocean is estimated to be 0.12° ± 0.02°C during 1960–2014, nearly threefold larger than that of the Indo-Pacific Oceans (0.035° ± 0.011°C and 0.035° ± 0.012°C for the Indian and Pacific Oceans, respectively) and ~70% larger than that of the Southern Ocean (0.070° ± 0.009°C). Although the Southern Ocean shows a weaker average warming rate than the Atlantic Ocean, it stands out with the strongest increase in ocean heat content (e.g., Cheng et al. 2022; Lyu et al. 2020).

The substantial warming of the Atlantic Ocean is also a salient feature in historical simulations of CMIP6 models (Fig. 2). The MMM of CMIP6 simulations, representing primarily the external radiative forcing effect, has reproduced the key features of the observed ΔT pattern (Fig. 2a). CMIP6 models tend to produce stronger warming in the subpolar oceans of the Northern Hemisphere and weaker warming in the subtropical Atlantic and the Southern Ocean than in observations. Nevertheless, CMIP6 MMM has reproduced well the interbasin warming contrasts, showing that the basin-average warming rate in the Atlantic is significantly higher than that in the other oceans (Fig. 2b). The consistency between observations and models suggests that the observed interbasin warming contrasts are primarily shaped by external forcing rather than internal variability. Here, the external forcing arises mainly from human activities, since the natural forcing by volcanic eruptions is identified to briefly change the ocean warming trend but plays a small role in the long-term change in ocean heat content (Gleckler et al. 2012; Balmaseda et al. 2013; Meehl et al. 2015). The Atlantic Ocean ΔT stood out from the others since the 1990s in CMIP6 MMM, with a total change of 0.10° ± 0.01°C during 1960–2014, slightly lower than the observed counterpart (0.12° ± 0.01°C). The observation–model difference arises partly from internal variabilities in the observations that have been largely removed in CMIP6 MMM. For example, the North Atlantic Oscillation (Sun et al. 2015) and Atlantic multidecadal oscillation (Sun et al. 2019) are known to modulate the warming pace of the Atlantic (Drijfhout et al. 2014; Robson et al. 2012; Lozier et al. 2008; Gulev et al. 2013).

The substantial warming in the Atlantic Ocean is of robustness in both observations and models. Given the uncertainties in observations due to poor data sampling before the Argo era, climate models appear more suitable to understand ocean warming since the mid-twentieth century. In the following, we seek possible mechanisms for the substantial warming of the Atlantic Ocean in response to anthropogenic climate change by analyzing CMIP6 simulations.

b. *The role of surface heat uptake*

First, we assess the ocean temperature change induced by the surface heat uptake, i.e., ΔT_{uptake}, by integrating surface net heat flux anomaly over 1960–2014 using the CMIP6 historical simulations (Fig. 3) based on the heat budget equation (section 2d). The ΔT_{uptake} pattern is characterized by enhanced heat uptake in the midlatitude oceans within the 30°–65° bands of both hemispheres, in contrast to the weak or even negative heat uptake in tropical oceans between 30°S and 30°N and the Arctic Ocean (Fig. 3a), which are consistent with previous studies (Hu et al. 2020; Marshall et al. 2015; G. Wang et al. 2015). Hotspots of surface heat uptake include the Gulf Stream, the subpolar North Atlantic except the Labrador Sea, the northwest Pacific along Kuroshio Extension, and the northern flank of the Antarctic Circumpolar Current in the Southern Ocean (Gregory et al. 2016; Ma et al. 2020). The strongest ΔT_{uptake} is found in the North Atlantic Ocean; the warming in the Gulf Stream, the North Atlantic Current, and the eastern subpolar gyre is close to 1°C (Fig. 3a). The ΔT_{uptake} integrated over the subtropical–subpolar North Atlantic (30°–68°N) accounts for 97% of the total ΔT_{uptake} of the entire Atlantic Ocean (34°S–68°N) and 38% of that of the global ocean. This confirms that the midlatitude North Atlantic is a major conduit for ocean surface heat uptake (Shi et al. 2018; Marshall et al. 2015). The Southern Ocean also plays an essential role in ocean heat uptake (Fig. 3a). The heat uptake integrated over the Southern Ocean exceeds that of the North Atlantic Ocean (Shi et al. 2018; Marshall et al. 2015).

The ΔT_{uptake} explains the majority of the interbasin contrasts in ΔT in CMIP6 MMM (Fig. 2b vs Fig. 3b). Like ΔT, the Atlantic ΔT_{uptake} stood out from others since the 1990s. The basin-average ΔT_{uptake} of the Atlantic Ocean is 0.10° ± 0.02°C during 1960–2014, close to the magnitude of ΔT (0.10° ± 0.01°C) and much larger

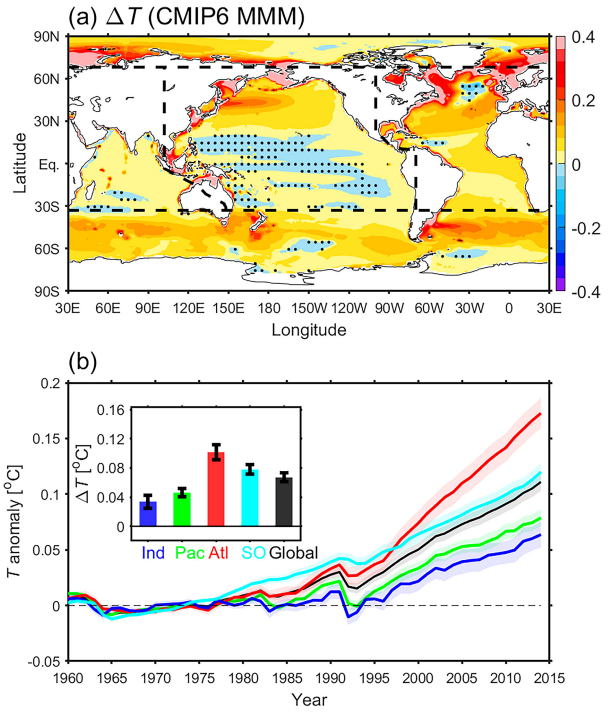

FIG. 2. (a) As in Fig. 1a, but for ΔT derived from the MMM of historical simulations from 24 CMIP6 models. (b) The 0–2000-m averaged ocean temperatures for the global ocean and individual ocean basins are derived from CMIP6 models and shown as anomalies relative to the 1960–80 baseline. Thick curves and shadings denote the ensemble mean and one standard error range of models, respectively. The inset in (b) shows the averaged ΔT for the global ocean and individual ocean basins from CMIP6 MMM, respectively, with the error bars showing one standard error range of models.

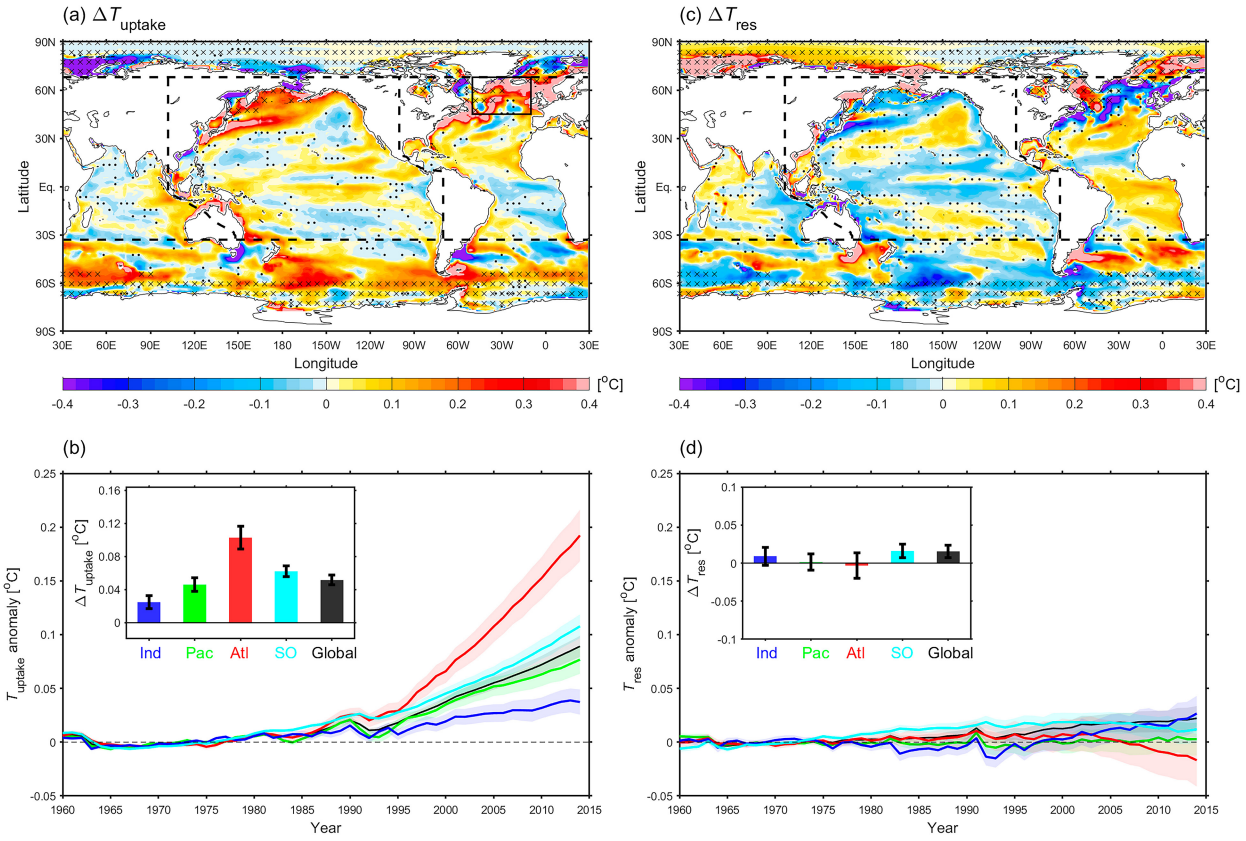

FIG. 3. (a) The 0–2000-m temperature changes induced by surface heat uptake (ΔT_{uptake}; °C) in CMIP6 MMM. The changes are computed as the difference between the 1994–2014 and 1960–80 periods. Stippling indicates the insignificant ΔT_{uptake} values at the 95% confidence level. The cross "×" marks the maximum extent of sea ice in the analyzed CMIP6 models. The black box shows the subpolar North Atlantic Ocean (10°–50°W, 45°–68°N). (b) The 0–2000-m averaged T_{uptake} anomalies for the global ocean and individual ocean basins derived from CMIP6 models (thick curve for MMM; shading for the one standard error), relative to the 1960–80 baseline. The inset shows the average ΔT_{uptake} for the global ocean and individual ocean basins with the error bars showing one standard error range of models. (c),(d) As in (a) and (b), but for the residual term ΔT_{res} (°C).

than those in other oceans. Therefore, surface heat uptake plays a central role in shaping the interbasin warming contrasts, and the enhanced surface heat uptake is the primary cause for the substantial Atlantic Ocean warming in CMIP6 models.

Note that sea ice insulates the ocean from direct air–sea heat fluxes; thus, the changes in sea ice coverage and ice–ocean heat flux would influence the ocean heat uptake at high latitudes, such as the Labrador Sea. The Q_{net} from the ocean models that are used in our calculation (section 2d) includes the ocean heat loss associated with sea ice melting/freezing. However, the heat flux into the ocean due to underwater frazil ice formation Q_{ice} is not included in Q_{net}. The Q_{ice} is available from only 10 models (Table 1). For those 10 models, we also calculated T_{uptake} by integrating Q_{net} plus Q_{ice} over time using Eq. (3) to examine the additional influence of underwater frazil ice formation on the ocean heat uptake, which turned out to be negligible (Fig. 3 and supplemental Fig. 1).

In addition to surface heat uptake, lateral heat flux convergence by ocean dynamical processes such as ocean circulation, eddy transport, and mixing, represented by the residual ΔT_{res}, also modulates regional warming rates (Fig. 3c). In hotspot regions with substantial surface heat uptake such as the Gulf Stream and northern flank of the Antarctic Circumpolar Current, ΔT_{res} tends to be locally negative. This indicates that ocean dynamical processes can transport the warming signatures produced by surface heat uptake elsewhere. The compensation between ΔT_{uptake} and ΔT_{res} also arises from the fact that temperature changes driven by ocean dynamics, such as advection by ocean circulation changes, e.g., the Labrador Sea, can be partly damped by the surface heat fluxes (Xie and Vallis 2012; Hu et al. 2020), and vice versa. Therefore, caution is required in the attribution of ΔT based on the relationship between ΔT_{uptake} and ΔT_{res}.

The heat redistribution drives regional warming in the Labrador Sea and the Nordic seas, the tropical–subtropical Atlantic, the Indian Ocean, and the Southern Ocean (Fig. 3c). In the Atlantic Ocean, the reduced northward meridional heat transport (MHT) induced by the slowdown of the AMOC causes a heat pileup in the South Atlantic (Zhu and Liu 2020) and a heat flux divergence in the North Atlantic (Figs. 4a–c). The

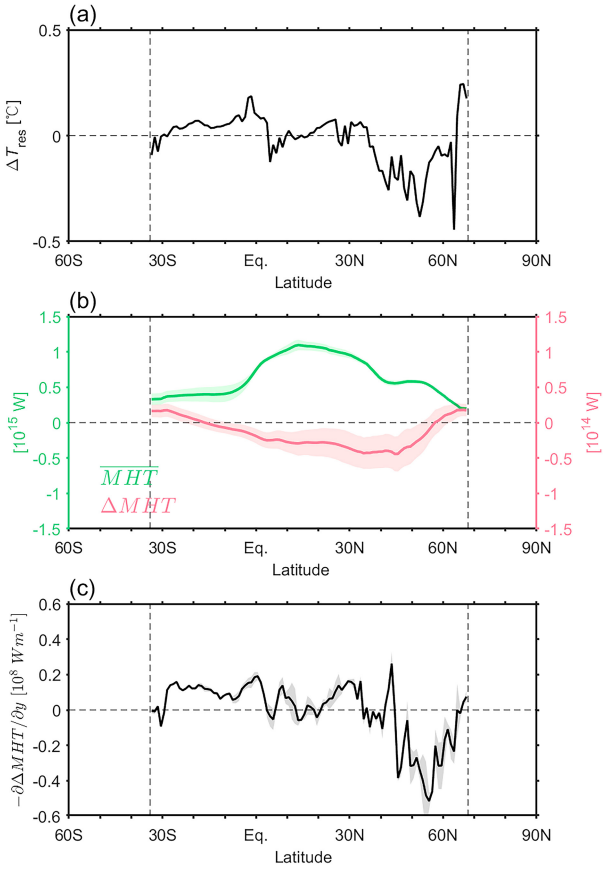

FIG. 4. (a) The Atlantic sector zonal-averaged ΔT_{res}, (b) the climatological annual-mean meridional heat transport ($\overline{MHT}$; 10^{15} W; green curve) during 1960–2014 and its change (ΔMHT; 10^{14} W; red curve), and (c) change in meridional heat flux convergence [$-(\partial\Delta MHT/\partial y)$; 10^8 W m^{-1}]. Thick curves and shadings in (b) and (c) denote the MMM and one standard error range, respectively, of the 14 CMIP6 models with MHT available. All changes are computed as the differences between the 1994–2014 and 1960–80 periods.

convergence of MHT explains a considerable portion of ΔT_{res} in the Atlantic Ocean, with a correlation coefficient of 0.69 (Fig. 4a vs Fig. 4c). This indicates that the AMOC slowdown overall leads to cooling in the subpolar North Atlantic and warming in the tropical and South Atlantic. However, this meridional transportation has limited contribution to the basin-averaged ΔT of the whole Atlantic Ocean and the interbasin warming contrasts (Fig. 3d).

We further analyze the changes in net surface heat flux ΔQ_{net} and its components to explore the causes of ΔT_{uptake} (Fig. 5). As shown in previous studies, ΔQ_{net} generally shows a similar pattern to ΔT_{uptake} (Ma et al. 2020; Hu et al. 2020). Two stark features arise from ΔQ_{net}: the meridional structure with enhanced increase in midlatitude (~30°–60°N and ~30°–60°S) oceans and the interbasin contrasts (Figs. 5a,b). This meridional structure of ΔQ_{net} is closely related to the spatial patterns of shortwave radiation change (ΔSWR) and turbulent heat flux change (ΔTHF). At low latitudes, the warming effect of longwave radiation change (ΔLWR) is greatly offset by the cooling effect of shortwave radiation change (Figs. 5e–h). At midlatitudes, both ΔSWR and ΔTHF contribute to the positive ΔQ_{net}.

In addition, ΔSWR and ΔTHF also synergistically result in the interbasin contrasts in ΔQ_{net}. The large ΔTHF in the subpolar North Atlantic and the increased ΔSWR in the subtropical–subpolar North Atlantic are responsible for the majority of the North Atlantic heat uptake (Figs. 5a,b and supplemental Fig. 2). The positive ΔLWR is slightly stronger in the low latitudes than in the midlatitudes and relatively uniform over the different oceans (Figs. 5e,f), reflecting the uniform distribution of greenhouse gases in the atmosphere. As a result, ΔLWR has a limited contribution to the meridional structure and interbasin contrasts in heat uptake. Although the changes in decomposed surface heat fluxes from atmospheric models (Figs. 5c–h) differ from those from the ocean model components (supplemental Fig. 3) in the sea ice covers regions, the basic features are similar.

c. *Processes responsible for the surface heat uptake*

We further explore the processes underlying ΔTHF and ΔSWR that are essential for the interbasin contrasts and meridional structures of surface heat uptake. The ΔTHF contains changes in sensible and latent heat flux (ΔSHF and ΔLHF). The ΔSHF is positive, indicative of suppressed SHF toward the atmosphere, in most parts of oceans and is enhanced in the subpolar North Atlantic (Fig. 6a). There is a maximum of positive ΔSHF emerging in the warming hole region. By contrast, positive ΔLHF values are mainly confined to the warming hole region, whereas the remnant of the Atlantic Ocean shows a negative ΔLHF (Fig. 6c). Both ΔSHF and ΔLHF contribute to the larger ΔTHF in the North Atlantic than in the North Pacific in the midlatitudes (Figs. 5c,d).

The ΔTHF is closely related to changes at the air–sea interface, such as the sea–air temperature difference δT (SST minus surface air temperature) and the specific humidity difference δq (air specific humidity at the sea surface minus air specific humidity at 10 m above the sea), as well as near-surface wind speed. Generally, increasing δT and δq act to enhance SHF and LHF release to the atmosphere in cold seasons, respectively. Owing to greenhouse warming, SST and air temperature have both warmed. However, the warming rate of air temperature is overall faster than that of SST in most regions, leading to a decline in δT and a positive ΔSHF (Figs. 6a,b). The decrease in δT generally strengthens with the increasing latitude, giving rise to enhanced positive ΔSHF in the subpolar oceans. The NAWH and waters around Antarctica show weaker SST warming than other regions and even regional cooling (Fig. 7a). The NAWH has been attributed to the slowdown of the AMOC (Caesar et al. 2018; Liu et al. 2020; Latif et al. 2022; Rahmstorf et al. 2015; Chemke et al. 2020) and changes in atmospheric circulation (He et al. 2022; Li et al. 2021; Hu and Fedorov 2020). Although small in the surface area, the cooling of the NAHW enhances the decrease in δT and contributes to the ΔSHF in the subpolar North Atlantic. Besides, SST cooling also works to reduce δq (Sun and Wu 2022). The decreasing δq in the subpolar North Atlantic suppresses LHF release to the atmosphere and accounts for the enhanced increase in ΔTHF there (Figs. 6c,d). Intermodel

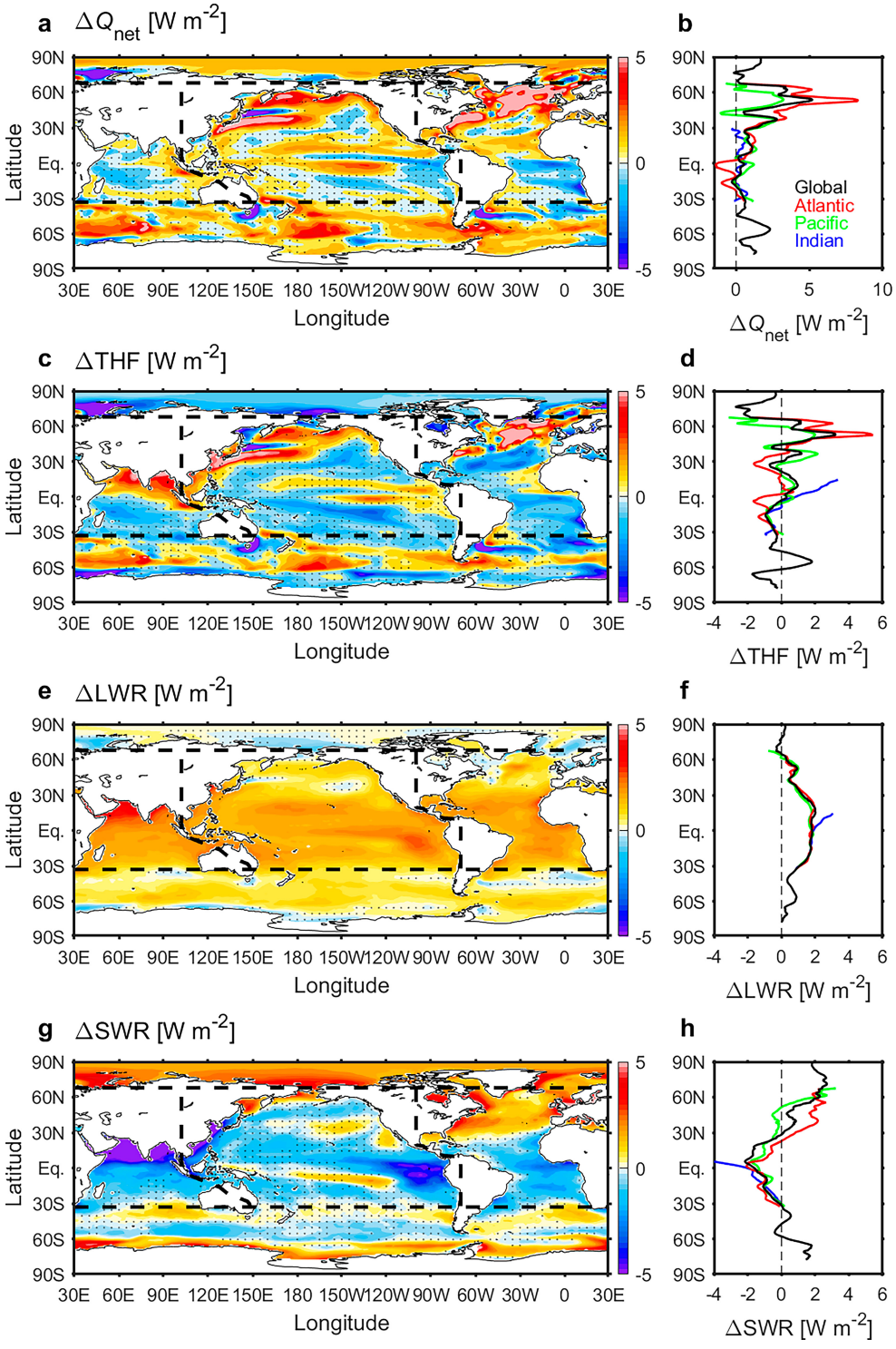

FIG. 5. Changes in (a) net surface heat flux ΔQ_{net}, (c) turbulent heat flux ΔTHF, (e) longwave radiation ΔLWR, and (g) shortwave radiation ΔSWR. Stippling indicates insignificant changes at the 95% confidence level. Zonal-averaged (b) ΔQ_{net}, (d) ΔTHF, (f) ΔLWR, and (h) ΔSWR in the global ocean and individual ocean basins. All variables are derived from the CMIP6 MMM and shown in W m^{-2}, with positive values indicating into the ocean. Note that the ΔQ_{net} is based on the ocean model outputs, while ΔTHF, ΔLWR, and ΔSWR used the atmospheric model outputs due to data availability (also see supplemental Fig. 3). Changes are computed as the differences between the 1994–2014 and 1960–80 periods.

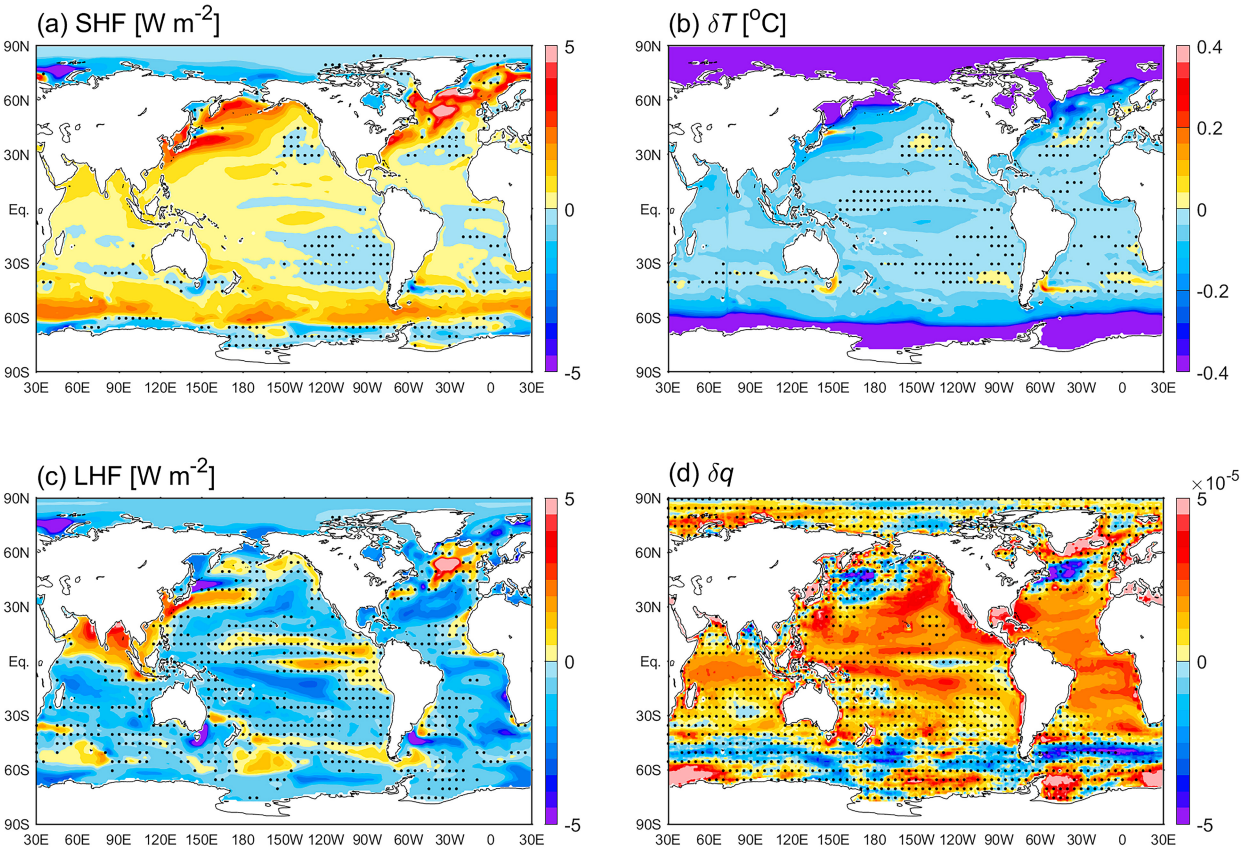

FIG. 6. Changes in (a) SHF (W m^{-2}), (b) near-surface sea–air temperature difference δT (°C), (c) LHF (W m^{-2}), and (d) specific humidity difference δq. All changes are computed as the differences between the 1994–2014 and 1960–80 periods. Stippling indicates insignificant changes at the 95% confidence level.

correlation confirms the close relationship between ΔSST and ΔTHF in the subpolar North Atlantic, with a correlation of $r = -0.63$ at a 99% confidence level (Fig. 7c). The warming signatures caused by surface heat uptake in the subpolar North Atlantic could be transported to lower latitudes by ocean circulations and contribute to the warming of the entire Atlantic Ocean.

The change in near-surface wind speed (ΔWS) also plays an important role in THF change. The reduction in near-surface wind speed also favors the reduction of SHF and LHF release and thereby enhances the increase in ΔTHF. CMIP6 models suggest a significant reduction in wind speed in the subtropical–subpolar band of the North Hemisphere (30°–70°N) and the Southern Hemisphere oceans between 35° and 50°S (Fig. 7b), which also accounts for the increase in ΔTHF. The intermodel correlation between ΔWS and ΔTHF in the subpolar North Atlantic is $r = -0.59$, significant at a 99% confidence level (Fig. 7d). Despite also weakened wind speed, the ΔTHF in the subpolar North Pacific is weaker than that in the North Atlantic counterpart owing to more substantial SST warming there (Fig. 7a).

The ΔSWR is intimately linked to changes in aerosol concentrations and total cloud cover of the atmosphere. Aerosols induce a net cooling through absorption and scattering of shortwave radiation (the direct effect) and changes in cloud microphysical properties (the indirect effect), showing opposing effects with the greenhouse gases (Shi et al. 2022; Deser et al. 2020). Aerosols are heterogeneous spatially and nonmonotonic temporally. Aerosol change during 1960–2014 is characterized by sharp decreases over North America and Europe and increases over Asia and Africa (Y. Wang et al. 2015; Shi et al. 2022), causing a decrease in aerosol concentration over the North Atlantic Ocean and an increase over midlatitude North Pacific Ocean, respectively (Fig. 8). Although the aerosol forcing in CMIP6 may be too large in some CMIP6 models and inconsistent with observations (Robson et al. 2022), the evolving spatial pattern of aerosol over the historical period is robust (Deser et al. 2020; Shi et al. 2022). The reductions of anthropogenic aerosols and cloud cover (Fig. 9a) over the North Atlantic synergistically drive the increase of solar radiation into the ocean and contribute to the enhanced heat uptake there. In the North Pacific, by contrast, the increased anthropogenic aerosols compensate for the reduced cloud cover, leading to the weak and insignificant ΔSWR there (Fig. 5g).

In addition to the processes contributing to the marked increase in ΔTHF and ΔSWR centered around the North Atlantic, the near-surface wind speed changes and cloud cover changes in a broader scale over the entire midlatitude result in the formation

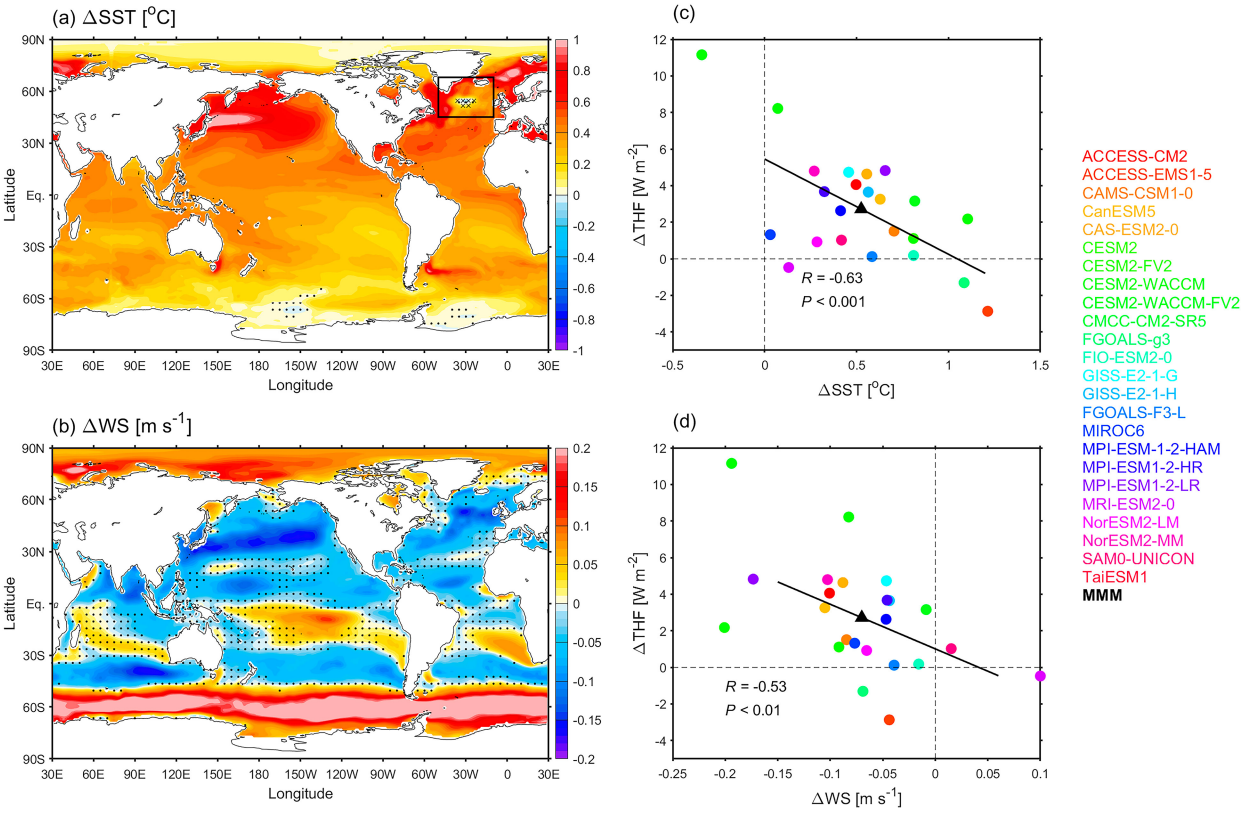

FIG. 7. Changes in (a) sea surface temperature ΔSST (°C) and (b) near-surface wind speed ΔWS (m s^{-1}). Stippling indicates insignificant changes at the 95% confidence level. Crosses "×" in (a) mark the extent of ΔSST < 0.2°C in the subpolar North Atlantic Ocean. All changes are computed as the differences between the 1994–2014 and 1960–80 periods. (c) Scatterplot of ΔSST vs ΔTHF over the subpolar North Atlantic Ocean [10°–50°W, 45°–68°N, black box in (a)] across CMIP6 models. The black triangle denotes the MMM. The correlation coefficient *r* with its *p* value and the linear fit (black solid line) are shown. (d) As in (c), but for scatterplot of ΔWS vs ΔTHF across CMIP6 models.

of overall meridional structure in ΔTHF and ΔSWR (Figs. 5d,h) and could contribute to the faster Atlantic warming indirectly through the effect of the basin shape (as explained in section 3d). The total cloud cover is reduced in the subtropical–subpolar band of the Northern Hemisphere (Fig. 9a), enhancing the solar radiation reaching the sea surface and contributing to the meridional structure of surface heat flux (Fig. 5h). The negative change in cloud cover (ΔCl) in the North Pacific and North Atlantic is

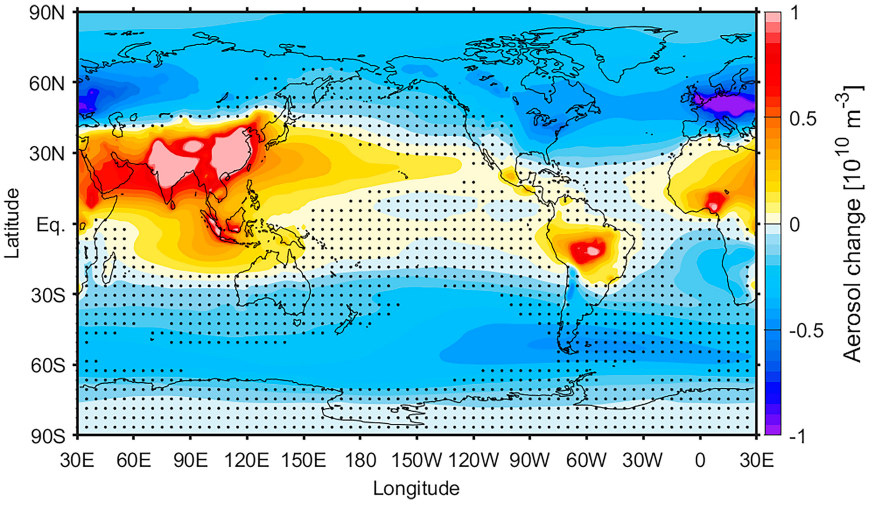

FIG. 8. Changes in total aerosol concentration (10^{10} m^{-3}) from the CMIP6 MMM. Stippling indicates insignificant changes at the 95% confidence level. All changes are computed as the differences between the 1994–2014 and 1960–80 periods.

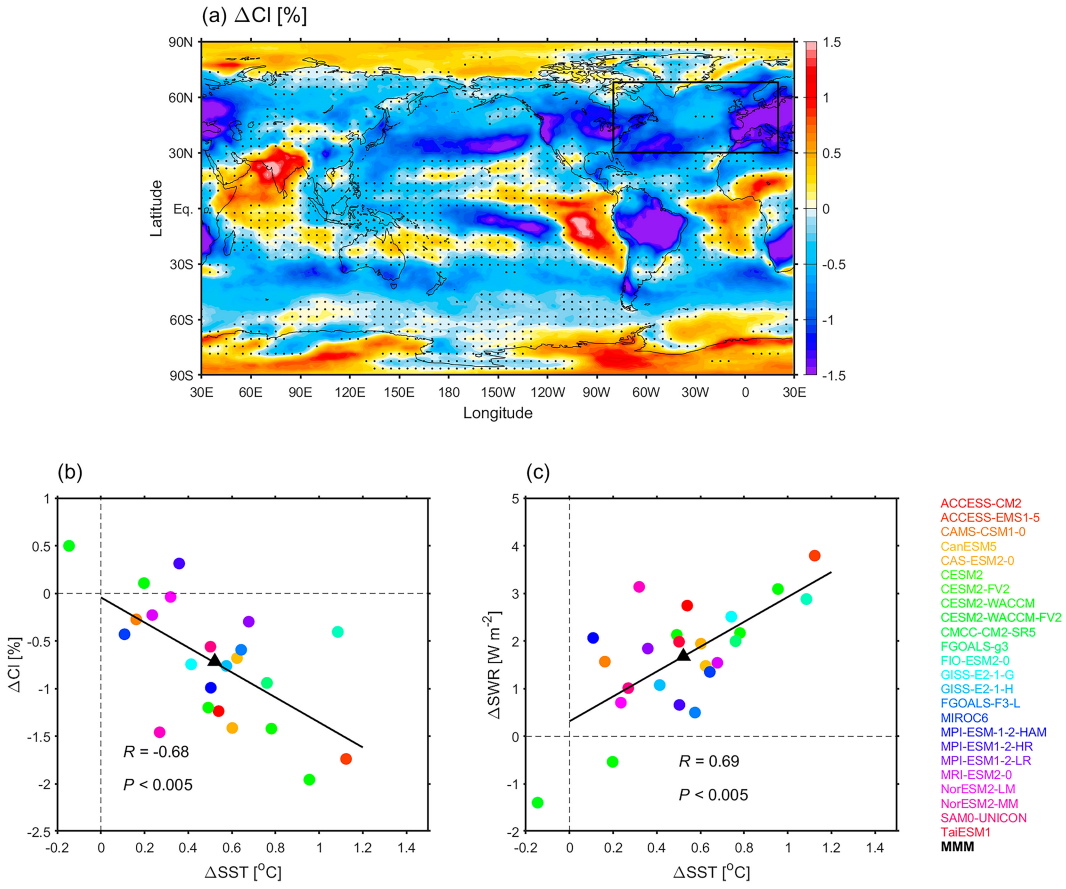

FIG. 9. (a) Changes in total cloud cover (ΔCl; %) from CMIP6 MMM. Stippling indicates insignificant changes at the 95% confidence level. (b) Scatterplot of ΔSST vs ΔCl over the subtropical and subpolar North Atlantic Ocean [20°E–80°W, 30°–68°N, black box in (a)] across CMIP6 models. The color of the circles matches the list of the model names in the far right column. The black triangle denotes the MMM. The correlation coefficient r with its p value and the linear fit (black solid line) are shown. (c) As in (b), but for scatterplot of ΔSST vs ΔSWR across CMIP6 models. All changes are computed as the differences between the 1994–2014 and 1960–80 periods.

mainly the manifestation of low cloud changes (Fig. 10a). Reduced low cloud cover and SST warming constitute a positive feedback loop (Park et al. 2006; Clement et al. 2009). The warmer SST destabilizes the lower troposphere and suppresses subsidence motion, releases more moisture out of the boundary layer, and lifts the cloud base, thereby decreasing the thermal and moisture coupling between the surface and the cloud layer (Park et al. 2006). This positive feedback among SST, low cloud, and SWR is consistent with the intermodel correlations among ΔSST, ΔCl, and ΔSWR over the subtropical and subpolar North Atlantic (Figs. 9b,c). The change of high cloud cover also contributes to the negative ΔCl in the 20°–40°N band of the North Hemisphere (Fig. 10b). This feature is linked to the poleward shift and intensification of the subtropical high (Li et al. 2012) and Hadley cell (Yang et al. 2020; Hu et al. 2013, 2018; Grise et al. 2019; Pikovnik et al. 2022; Power et al. 2021) in the Northern Hemisphere under greenhouse warming (Figs. 10c,d). These alterations in atmospheric circulation enhance the subsidence motion in the subtropical regions, resulting in the reduction of high cloud cover there (Fig. 10b).

Furthermore, the reductions in wind speed in the subtropical–subpolar band of the North Hemisphere and the Southern Ocean within 30°–50°S suppress the reduction of THF release to the atmosphere. The reduction in near-surface wind speed also favors the reduction of the air–sea temperature differences (He et al. 2022), which is conducive to the formation of meridional structure in ΔSHF (Fig. 6a). The broadscale changes in near-surface wind speed in CMIP6 simulations are partly linked to alterations in atmospheric circulation and storm tracks in response to external forcing (Deng et al. 2021; Li et al. 2021; Gonzalez et al. 2019; Chang and Yau 2016). The poleward shift of westerly jet streams has led to the weakening of zonal winds over the midlatitude North Pacific and Atlantic Oceans (Fig. 11), contributing to the reduction of wind speed (Yang et al. 2020, 2022; Gonzalez et al. 2019). The change in wind speed cannot be explained by changes in large-scale circulation alone because the surface wind speed is transient and affected by local boundary layer processes (Gonzalez et al. 2019; Zeng et al. 2019).

In summary, the alterations of large-scale atmospheric circulation under greenhouse warming are essential for the meridional

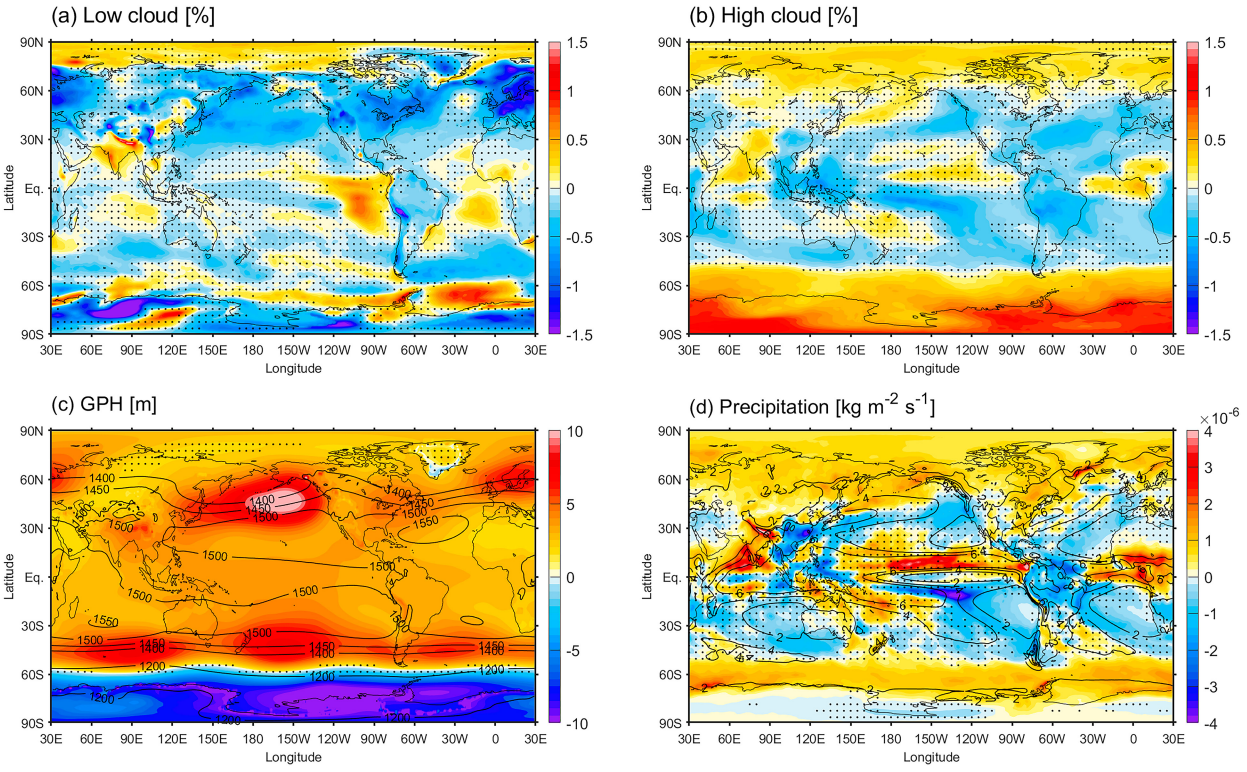

FIG. 10. (a) Changes in low cloud cover percentage (%), (b) high cloud cover percentage (%), (c) GPH at 850 hPa (m), and (d) precipitation (kg m^{-2} s^{-1}). Black contours in (c) and (d) are the climatological GPH at 850 hPa and precipitation (10^5 kg m^{-2} s^{-1}) during 1960–80, respectively. Stippling indicates insignificant changes at the 95% confidence level. All changes are the differences between the 1994–2014 and 1960–80 periods in the CMIP6 MMM.

structure of surface heat uptake, leading to broadly enhanced surface heat flux in midlatitude oceans through the reduced near-surface wind speed and cloud cover. Weak SST warming in the subpolar North Atlantic and the reduced anthropogenic aerosol concentration in the North Atlantic contribute to the enhanced heat uptake in the North Atlantic Ocean through suppressing the THF release to the atmosphere and enhancing SWR into the ocean, respectively. The enhanced surface heat uptake in the subtropical and subpolar North Atlantic naturally contributes to the much higher average heat uptake in the Atlantic Ocean overall. Additionally, the meridional structure of surface heat uptake is conducive to greater warming in the Atlantic due to the geographical factor, which is discussed in the following subsection.

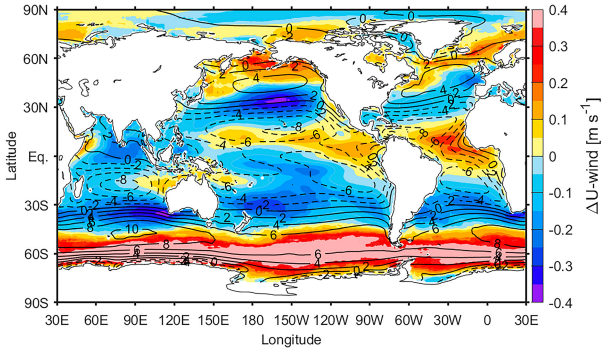

FIG. 11. Changes in near-surface zonal wind ΔU wind (color shading; m s^{-1}) from the CMIP6 MMM. The contours indicate the climatological U wind (m s^{-1}) during 1960–2014. All changes are computed as the differences between the 1994–2014 and 1960–80 periods.

d. *Additional effect of the geographic shape of the ocean basins*

Here, we have addressed the contributions of basin-average surface heat uptake to temperature changes in the 0–2000 m in individual oceans. As shown in Eq. (1), the basin-averaged heat uptake also depends on the relative area weight of high/low amplitude heat uptake regions $\Delta A/\int dA$, in addition to the amplitude of local ΔT_{uptake}.

The ΔT_{uptake} pattern in Fig. 3a shows the meridional structure with overall higher heat uptake in the midlatitude Northern Hemisphere than in the low-latitude oceans, in addition to the fact that the heat uptake in the North Atlantic Ocean is higher than that in the North Pacific. Moreover, the width of the Atlantic basin is comparable between mid- and low latitudes, while the Indo-Pacific Oceans are much wider in low latitudes than in midlatitudes (Fig. 12a). Consequently, a relatively larger portion of the North Atlantic area has been exposed to enhanced heat uptake in midlatitudes than in the North Pacific Ocean (Fig. 12b). The midlatitude North Pacific poleward of 30°N makes up only ~19% of the total area of the Pacific Ocean, whereas this ratio is

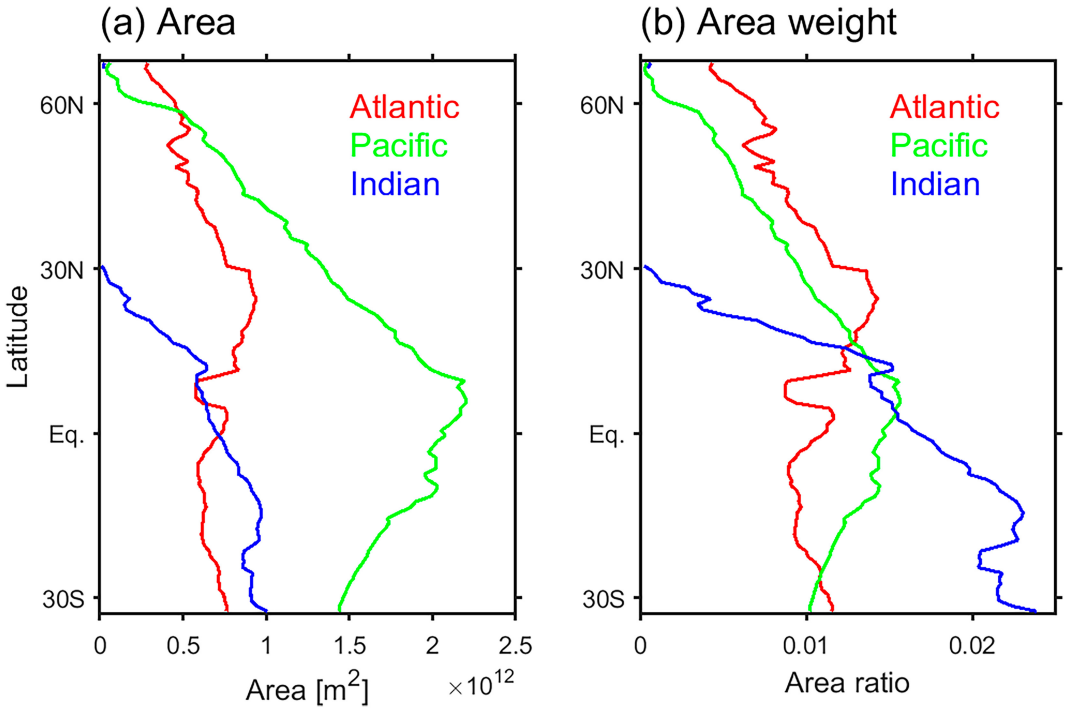

FIG. 12. (a) Zonally integrated area of individual oceans in the band of 33°S–68°N, with the latitude bin of 1°. (b) The latitude-dependence area weight of individual oceans, which is the zonally integrated area within each ocean divided by the total area of the corresponding ocean.

as high as ~31% for the Atlantic Ocean; the low-latitude Pacific Ocean within 30°S–30°N with low heat uptake accounts for as large as ~78% of the entire Pacific, whereas this ratio is only ~65% in the Atlantic Ocean. Therefore, it is the combination of the meridional structure of the overall ΔT_{uptake} pattern and the geographic shape of the Atlantic Ocean that gives rise to an additional contribution to a higher basin-average heat uptake in the Atlantic Ocean than that in the Indo-Pacific Oceans.

This issue can be further elucidated by eliminating interbasin contrasts in ΔQ_{net} and highlighting the role of basin shapes and meridional structure of ΔQ_{net}. We recompute surface heat uptake by replacing Q_{net} anomaly at each grid point with the global zonal mean Q_{net} anomaly for the corresponding latitude, i.e., $\Delta T_{\text{uptake-ZM}}$, which ignores the dependence of Q_{net} change on longitude and highlights the dependence on latitude (Fig. 13a). The resulted $\Delta T_{\text{uptake-ZM}}$ shows the basic feature of the meridional structure of heat uptake pattern, with higher heat uptake in the midlatitude than in the low-latitude oceans. The $\Delta T_{\text{uptake-ZM}}$ of the Atlantic Ocean still stands out from those of other oceans (Fig. 13b), with the interbasin contrasts broadly resembling ΔT and ΔT_{uptake} (Figs. 2b and 3b). One may argue that the strongest increase in surface heat flux over the North Atlantic Ocean, which has been attributed to the AMOC slowdown, may influence the global zonal mean Q_{net} anomaly and then $\Delta T_{\text{uptake-ZM}}$. Here, we repeat the same analysis by excluding the Atlantic contribution to the zonal mean Q_{net} anomaly and show the response in ocean heat uptake $\Delta T_{\text{uptake-ZM-nonAtl}}$ in Fig. 13c. Although the $\Delta T_{\text{uptake-ZM-nonAtl}}$ is weaker than $\Delta T_{\text{uptake-ZM}}$ in the midlatitude Northern Hemisphere (Fig. 13c), the interbasin contrasts still exist with the largest basin-average $\Delta T_{\text{uptake-ZM-nonAtl}}$ in the Atlantic Ocean (Fig. 13d). This implies that as long as the Q_{net} anomalies are amplified in midlatitudes, the averaged surface heat uptake in the Atlantic Ocean would remain higher than that in the Indo-Pacific Oceans with or without the impact of the AMOC slowdown.

4. Conclusions and discussion

This study attributes the substantial warming of the whole Atlantic Ocean since the mid-twentieth century primarily to the excessive surface heat uptake through surface heat fluxes, based on analysis of CMIP6 model simulations. The observed 0–2000-m warming is nearly threefold stronger in the Atlantic Ocean than in the Indo-Pacific Oceans. The CMIP6 simulations indicate the dominance of externally forced surface heat uptake in shaping these interbasin contrasts in warming pace. More specifically, the surface heat uptake is responsible for the concentrated warming along the Gulf Stream, North Atlantic Current, and eastern North Atlantic, as well as the weaker warming in the subtropical North Atlantic. On the other hand, the ocean lateral heat flux convergence drives concentrated warming in the Labrador Sea, in addition to the broad warming in the South Atlantic and tropical/subtropical North Atlantic.

The surface heat uptake changes can be driven by both the changes in the ocean and atmospheric circulation. While the role of ocean circulation can be implied by the collocation of the concentrated surface heat uptake changes and the strong ocean currents, e.g., the Gulf Stream and the North Atlantic Current, changes in the atmospheric circulation also play a role. The weak

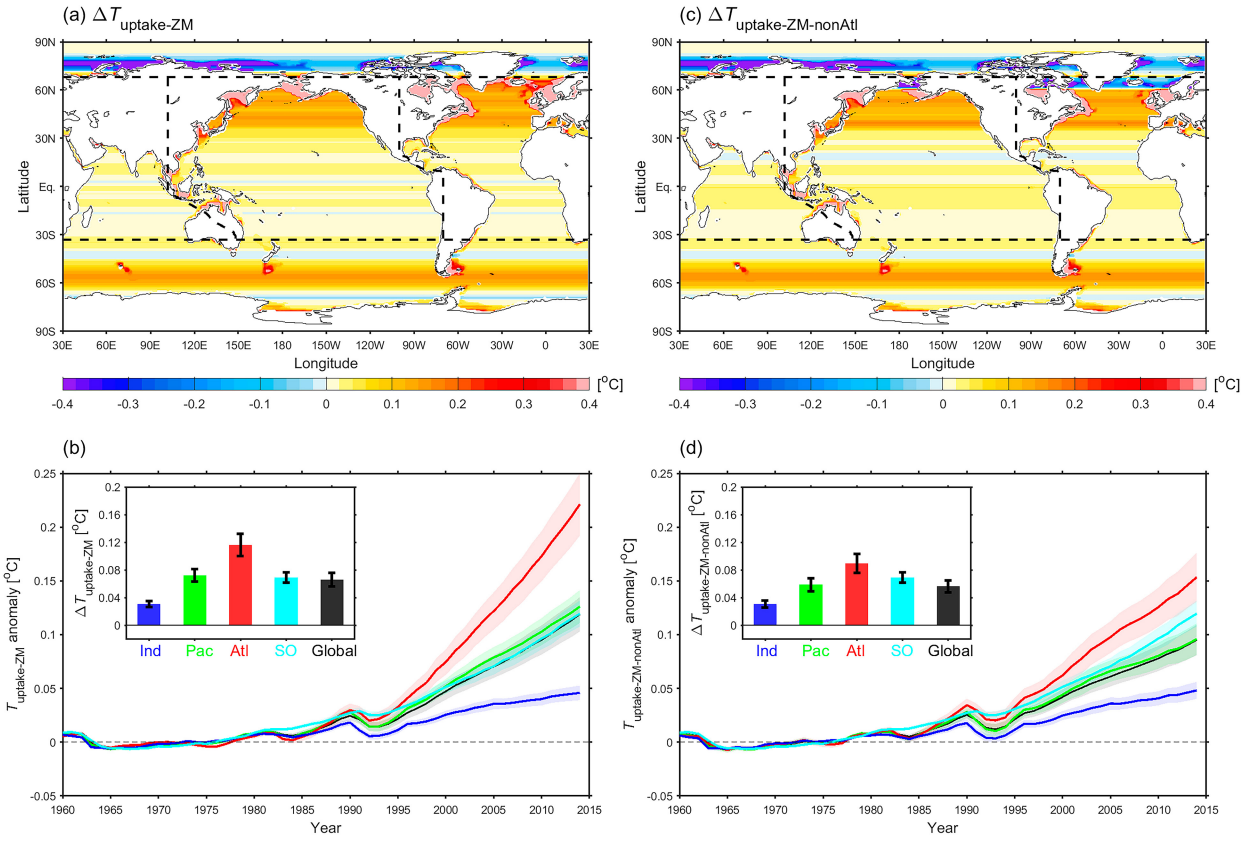

FIG. 13. (a) The 0–2000-m temperature changes induced by global zonal mean surface heat uptake $\Delta T_{\text{uptake-ZM}}$ (°C) in CMIP6 MMM. The change is computed as the difference between the 1994–2014 and 1960–80 periods. (b) The 0–2000-m averaged $T_{\text{uptake-ZM}}$ anomalies for the global ocean and individual ocean basins derived from CMIP6 models (thick curve for MMM; shading for the one standard error), relative to the 1960–80 baseline. The inset shows the average $\Delta T_{\text{uptake-ZM}}$ for the global ocean and individual ocean basins with the error bars showing one standard error range of models. (c),(d) As in (a) and (b), but for the temperature changes induced by non-Atlantic zonal mean surface heat uptake $\Delta T_{\text{uptake-ZM-nonAtl}}$.

SST warming even cooling in the subpolar North Atlantic and reduced anthropogenic aerosols in the North Atlantic significantly elevate the heat uptake in the North Atlantic Ocean. In addition, the weakening of near-surface wind speed and the decreasing total cloud cover over the midlatitude oceans give rise to enhanced heat uptake in the midlatitude Northern Hemisphere oceans as compared with that in the low-latitude oceans. These processes collectively result in a much greater heat uptake in the North Atlantic. Furthermore, the Atlantic Ocean, in contrast to the Indo-Pacific Oceans, is relatively wide in midlatitudes as compared to low latitudes and thus is proportionally more exposed to enhanced heat uptakes. This geographical factor and meridional structure of heat uptake work synergistically to result in a far larger basin-average heat uptake in the Atlantic Ocean and therefore stronger warming than in the Indo-Pacific Oceans.

The projection by CMIP6 models in three emission scenarios is further analyzed (Fig. 14). While the heat storage ΔT and heat uptake ΔT_{uptake} increase with the emission levels, the warming of the Atlantic Ocean is always the largest among all oceans. The dominance of heat uptake to ocean warming depends on the emission scenarios: heat uptake plays a more important role under higher emission levels, particularly for the Atlantic Ocean. This suggests that the enhanced warming of the Atlantic will probably persist in the upcoming decades unless the emission level can be slashed soon. This result is consistent with the previous studies that suggested that the Atlantic Ocean shows a higher degree of thermal sensitivity to the radiative forcing by anthropogenic greenhouse gases than other oceans (Shi et al. 2018; Ma et al. 2020). The continuously enhanced heat uptake and rapid warming of the North Atlantic, along with the resultant ice melting (Straneo and Heimbach 2013), would increase the potential for the abrupt AMOC collapse as a "low-probability, high-impact" event in the future (Liu et al. 2020; Cheng et al. 2022).

Our findings highlight the importance of surface heat fluxes in the interbasin contrasts of warming pace in CMIP6 models. However, due to the substantial uncertainties in the observed heat fluxes, in particular before the satellite era since the early 1980s (Armour et al. 2016), the realism of heat uptake changes in climate models cannot be assessed reliably against the observation. Albeit with detailed discrepancies, ensemble-mean changes of CMIP6 models in SST, surface air temperature, near-surface winds, and aerosols are largely in line with observational and reanalysis datasets over the North Atlantic (supplemental Fig. 4)

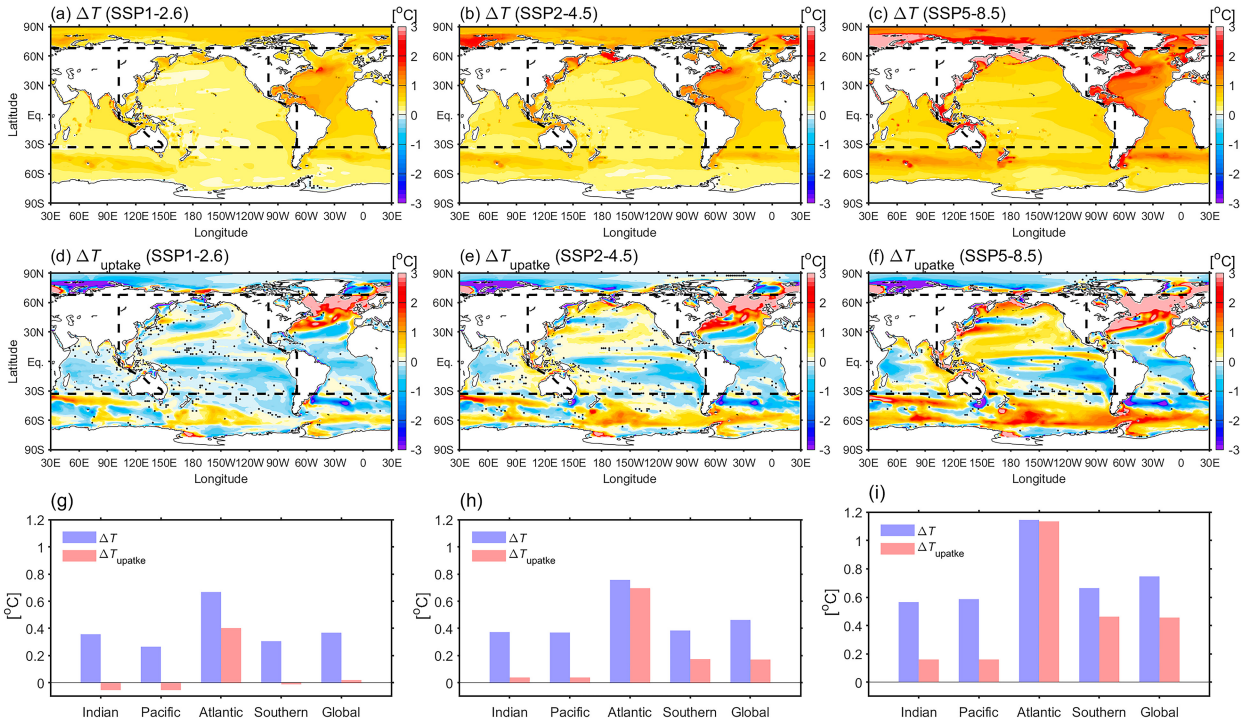

FIG. 14. The 0–2000 m ΔT (°C) from the MMM of (a) CMIP6 SSP1-2.6, (b) SSP2-4.5, and (c) SSP5-8.5 models (c). (d)–(f) As in (a)–(c), but for ΔT_{uptake} (°C). (g)–(i) As in (a)–(c), but for the averaged ΔT (blue) and ΔT_{uptake} (pink) for the global ocean and individual ocean basins. All changes are calculated as the differences between the 2080–2100 and 2015–35 periods. Stippling denotes the insignificant changes at the 95% confidence level.

(Yang et al. 2020, 2022; Li et al. 2012; Hu et al. 2013, 2018; Grise et al. 2019; Pikovnik et al. 2022; Power et al. 2021; Shi et al. 2022), pointing to the dominance of external forcing in historical changes. These consistencies place additional confidence in the simulated and projected heat uptake. The key factors controlling the surface heat uptake identified here, such as wind speed and SST of the midlatitude North Atlantic, are potentially useful in reducing uncertainties in model ensemble projection through the emergent constrain technique (Hall et al. 2019).

The heat uptake pattern is subjected to dynamical complexity of the climate system (Shi et al. 2018). While changes in atmospheric conditions play a role in shaping the meridional distribution of surface heat uptake, the enhanced surface heat uptake in the North Atlantic and the Southern Ocean is largely favored by ocean deep convection that efficiently conveys the warming signatures to the deep ocean (e.g., Shi et al. 2018; Gregory et al. 2016; Gulev et al. 2013). This process is lacking in the Indian and Pacific Oceans. Further efforts are required to achieve understanding of this critical issue.

Acknowledgments. We thank three anonymous reviewers who provided insightful comments. We gratefully acknowledge the support by the National Key R&D Program of China (2019YFA0606702), the Strategic Priority Research Program of Chinese Academy of Sciences (XDB40000000), the Laoshan Laboratory (LSKJ202202601), and the Oceanographic Data Center, the Institute of Oceanology, Chinese Academy of Sciences. Q. R. is supported by the Shandong Postdoctoral Innovation Program (E2KY291) and the National Natural Science Foundation of China for Young Scholar (42306037). Y.-O. K. is also supported by the U.S. National Science Foundation Physical Oceanography Program (OCE-2048336).

Data availability statement. All the datasets utilized in this study are publicly available through the following links: Argo (http://www.jamstec.go.jp/ARGO/J_ARGOe.html); IAP (http://www.ocean.iap.ac.cn/pages/dataService/dataService.html?navAnchor=dataService); Ishii V7.2 (https://climate.mri-jma.go.jp/pub/ocean/ts/); EN4.2.0 (https://www.metoffice.gov.uk/hadobs/en4/); Pentad WOA18 (https://www.nodc.noaa.gov/OC5/3M_HEAT_CONTENT/); the CMIP6 model outputs are available from the World Climate Research Programme (https://esgf-node.llnl.gov/search/cmip6/).

REFERENCES

Armour, K. C., J. Marshall, J. R. Scott, A. Donohoe, and E. R. Newsom, 2016: Southern Ocean warming delayed by circumpolar upwelling and equatorward transport. *Nat. Geosci.*, **9**, 549–554, https://doi.org/10.1038/ngeo2731.

Backeberg, B. C., P. Penvin, and M. Rouault, 2012: Impact of intensified Indian Ocean winds on mesoscale variability in the Agulhas system. *Nat. Climate Change*, **2**, 608–612, https://doi.org/10.1038/nclimate1587.

Balaguru, K., and Coauthors, 2023: Increased U.S. coastal hurricane risk under climate change. *Sci. Adv.*, **9**, eadf0259, https://doi.org/10.1126/sciadv.adf0259.

Balmaseda, M. A., K. E. Trenberth, and E. Källén, 2013: Distinctive climate signals in reanalysis of global ocean heat content. *Geophys. Res. Lett.*, **40**, 1754–1759, https://doi.org/10.1002/grl.50382.

Banks, H. T., and J. M. Gregory, 2006: Mechanisms of ocean heat uptake in a coupled climate model and the implications for tracer based predictions of ocean heat uptake. *Geophys. Res. Lett.*, **33**, L07608, https://doi.org/10.1029/2005GL025352.

Beal, L. M., W. P. M. De Ruijter, A. Biastoch, R. Zahn, and SCOR/WCRP/IAPSO Working Group 136, 2011: On the role of the Agulhas system in ocean circulation and climate. *Nature*, **472**, 429–436, https://doi.org/10.1038/nature09983.

——, S. Elipot, A. Houk, and G. M. Leber, 2015: Capturing the transport variability of a western boundary jet: Results from the Agulhas Current Time-series experiment (ACT). *J. Phys. Oceanogr.*, **45**, 1302–1324, https://doi.org/10.1175/JPO-D-14-0119.1.

Boers, N., 2021: Observation-based early-warning signals for a collapse of the Atlantic Meridional Overturning Circulation. *Nat. Climate Change*, **11**, 680–688, https://doi.org/10.1038/s41558-021-01097-4.

Boyce, D. G., M. R. Lewis, and B. Worm, 2010: Global phytoplankton decline over the past century. *Nature*, **466**, 591–596, https://doi.org/10.1038/nature09268.

Bronselaer, B., and L. Zanna, 2020: Heat and carbon coupling reveals ocean warming due to circulation changes. *Nature*, **584**, 227–233, https://doi.org/10.1038/s41586-020-2573-5.

Caesar, L., S. Rahmstorf, A. Robinson, G. Feulner, and V. Saba, 2018: Observed fingerprint of a weakening Atlantic Ocean overturning circulation. *Nature*, **556**, 191–196, https://doi.org/10.1038/s41586-018-0006-5.

Cai, W., and Coauthors, 2019: Pantropical climate interactions. *Science*, **363**, eaav4236, https://doi.org/10.1126/science.aav4236.

Chang, E. K. M., and A. M. W. Yau, 2016: Northern Hemisphere winter storm track trends since 1959 derived from multiple reanalysis datasets. *Climate Dyn.*, **47**, 1435–1454, https://doi.org/10.1007/s00382-015-2911-8.

Chemke, R., L. Zanna, and L. M. Polvani, 2020: Identifying a human signal in the North Atlantic warming hole. *Nat. Commun.*, **11**, 1540, https://doi.org/10.1038/s41467-020-15285-x.

Chen, X., and K. K. Tung, 2014: Varying planetary heat sink led to global-warming slowdown and acceleration. *Science*, **345**, 897–903, https://doi.org/10.1126/science.1254937.

——, and ——, 2018: Global surface warming enhanced by weak Atlantic overturning circulation. *Nature*, **559**, 387–391, https://doi.org/10.1038/s41586-018-0320-y.

Cheng, L., and J. Zhu, 2014: Artifacts in variations of ocean heat content induced by the observation system changes. *Geophys. Res. Lett.*, **41**, 7276–7283, https://doi.org/10.1002/2014GL061881.

——, K. E. Trenberth, J. Fasullo, T. Boyer, J. Abraham, and J. Zhu, 2017: Improved estimates of ocean heat content from 1960 to 2015. *Sci. Adv.*, **3**, e1601545, https://doi.org/10.1126/sciadv.1601545.

——, and Coauthors, 2022: Past and future ocean warming. *Nat. Rev. Earth Environ.*, **3**, 776–794, https://doi.org/10.1038/s43017-022-00345-1.

Clement, A. C., R. Burgman, and J. R. Norris, 2009: Observational and model evidence for positive low-level cloud feedback. *Science*, **325**, 460–464, https://doi.org/10.1126/science.1171255.

Deng, K., C. Azorin-Molina, L. Minola, G. Zhang, and D. Chen, 2021: Global near-surface wind speed changes over the last decades revealed by reanalyses and CMIP6 model simulations. *J. Climate*, **34**, 2219–2234, https://doi.org/10.1175/JCLI-D-20-0310.1.

Deser, C., and Coauthors, 2020: Isolating the evolving contributions of anthropogenic aerosols and greenhouse gases: A new CESM1 large ensemble community resource. *J. Climate*, **33**, 7835–7858, https://doi.org/10.1175/JCLI-D-20-0123.1.

Dias, F. B., and Coauthors, 2020: Ocean heat storage in response to changing ocean circulation processes. *J. Climate*, **33**, 9065–9082, https://doi.org/10.1175/JCLI-D-19-1016.1.

Drijfhout, S. S., A. T. Blaker, S. A. Josey, A. J. G. Nurser, B. Sinha, and M. A. Balmaseda, 2014: Surface warming hiatus caused by increased heat uptake across multiple ocean basins. *Geophys. Res. Lett.*, **41**, 7868–7874, https://doi.org/10.1002/2014GL061456.

Duan, J., Y. Li, L. Cheng, P. Lin, and F. Wang, 2023: Heat storage in the upper Indian Ocean: The role of wind-driven redistribution. *J. Climate*, **36**, 2221–2242, https://doi.org/10.1175/JCLI-D-22-0534.1.

Durack, P. J., P. J. Gleckler, F. W. Landerer, and K. E. Taylor, 2014: Quantifying underestimates of long-term upper-ocean warming. *Nat. Climate Change*, **4**, 999–1005, https://doi.org/10.1038/nclimate2389.

Eyring, V., S. Bony, G. A. Meehl, C. A. Senior, B. Stevens, R. J. Stouffer, and K. E. Taylor, 2016: Overview of the Coupled Model Intercomparison Project Phase 6 (CMIP6) experimental design and organization. *Geosci. Model Dev.*, **9**, 1937–1958, https://doi.org/10.5194/gmd-9-1937-2016.

Ferster, B. S., A. Simon, A. Fedorov, J. Mignot, and E. Guilyardi, 2022: Slowdown and recovery of the Atlantic meridional overturning circulation and a persistent North Atlantic warming hole induced by Arctic sea ice decline. *Geophys. Res. Lett.*, **49**, e2022GL097967, https://doi.org/10.1029/2022GL097967.

Frederikse, T., and Coauthors, 2020: The causes of sea-level rise since 1900. *Nature*, **584**, 393–397, https://doi.org/10.1038/s41586-020-2591-3.

Frölicher, T. L., E. M. Fischer, and N. Gruber, 2018: Marine heatwaves under global warming. *Nature*, **560**, 360–364, https://doi.org/10.1038/s41586-018-0383-9.

Fu, Y., L. Feili, J. Karstensen, and C. Wang, 2020: A stable Atlantic Meridional Overturning Circulation in a changing North Atlantic Ocean since the 1990s. *Sci. Adv.*, **6**, eabc7836, https://doi.org/10.1126/sciadv.abc7836.

Garuba, O. A., and B. A. Klinger, 2016: Ocean heat uptake and interbasin transport of the passive and redistributive components of surface heating. *J. Climate*, **29**, 7507–7527, https://doi.org/10.1175/JCLI-D-16-0138.1.

——, and ——, 2018: The role of individual surface flux components in the passive and active ocean heat uptake. *J. Climate*, **31**, 6157–6173, https://doi.org/10.1175/JCLI-D-17-0452.1.

Giannini, A., and A. Kaplan, 2019: The role of aerosols and greenhouse gases in Sahel drought and recovery. *Climatic Change*, **152**, 449–466, https://doi.org/10.1007/s10584-018-2341-9.

Gleckler, P. J., and Coauthors, 2012: Human-induced global ocean warming on a multidecadal timescales. *Nat. Climate Change*, **2**, 524–529, https://doi.org/10.1038/nclimate1553.

Gonzalez, P. L. M., D. J. Brayshaw, and G. Zappa, 2019: The contribution of North Atlantic atmospheric circulation shifts to future wind speed projections for wind power over Europe. *Climate Dyn.*, **53**, 4095–4113, https://doi.org/10.1007/s00382-019-04776-3.

Good, S. A., 2016: The impact of observational sampling on time series of global 0–700 m ocean average temperature: A case study. *Int. J. Climatol.*, **37**, 2260–2268, https://doi.org/10.1002/joc.4654.

——, M. J. Martin, and N. A. Rayner, 2013: EN4: Quality controlled ocean temperature and salinity profiles and monthly objective analyses with uncertainty estimates. *J. Geophys. Res. Oceans*, **118**, 6704–6716, https://doi.org/10.1002/2013JC009067.

Graham, T., and M. Vellinga, 2013: Heat budget of the upper Arctic Ocean under a warming climate. *Climate Dyn.*, **40**, 143–153, https://doi.org/10.1007/s00382-012-1454-5.

Gregory, J. M., and Coauthors, 2016: The Flux-Anomaly-Forced Model Intercomparison Project (FAFMIP) contribution to CMIP6: Investigation of sea-level and ocean climate change in response to CO_2 forcing. *Geosci. Model Dev.*, **9**, 3993–4017, https://doi.org/10.5194/gmd-9-3993-2016.

Grise, K. M., and Coauthors, 2019: Recent tropical expansion: Natural variability or forced response? *J. Climate*, **32**, 1551–1571, https://doi.org/10.1175/JCLI-D-18-0444.1.

Grist, J. P., and Coauthors, 2010: The roles of surface heat flux and ocean heat transport convergence in determining Atlantic Ocean temperature variability. *Ocean Dyn.*, **60**, 771–790, https://doi.org/10.1007/s10236-010-0292-4.

Gulev, S. K., M. Latif, N. Keenlyside, W. Park, and K. P. Koltermann, 2013: North Atlantic Ocean control on surface heat flux on multi-decadal timescales. *Nature*, **499**, 464–467, https://doi.org/10.1038/nature12268.

Hall, A., P. Cox, C. Huntingford, and S. Klein, 2019: Progressing emergent constraints on future climate change. *Nat. Climate Change*, **9**, 269–278, https://doi.org/10.1038/s41558-019-0436-6.

He, C., A. C. Clement, M. A. Cane, L. N. Murphy, J. M. Klavans, and T. M. Fenske, 2022: A North Atlantic warming hole without ocean circulation. *Geophys. Res. Lett.*, **49**, e2022GL100420, https://doi.org/10.1029/2022GL100420.

Hirasawa, H., P. J. Kushner, M. Sigmond, J. Fyfe, and C. Deser, 2020: Anthropogenic aerosols dominate forced multidecadal Sahel precipitation change through distinct atmospheric and oceanic drivers. *J. Climate*, **33**, 10 187–10 204, https://doi.org/10.1175/JCLI-D-19-0829.1.

Hu, S., and A. V. Fedorov, 2020: Indian Ocean warming as a driver of the North Atlantic warming hole. *Nat. Commun.*, **11**, 4785, https://doi.org/10.1038/s41467-020-18522-5.

——, S.-P. Xie, and W. Liu, 2020: Global pattern formation of net ocean surface heat flux response to greenhouse warming. *J. Climate*, **33**, 7503–7522, https://doi.org/10.1175/JCLI-D-19-0642.1.

Hu, Y., T. Lijun, and L. Jiping, 2013: Poleward expansion of the Hadley circulation in CMIP5 simulations. *Adv. Atmos. Sci.*, **30**, 790–795, https://doi.org/10.1007/s00376-012-2187-4.

——, H. Huang, and C. Zhou, 2018: Widening and weakening of the Hadley circulation under global warming. *Sci. Bull.*, **63**, 640–644, https://doi.org/10.1016/j.scib.2018.04.020.

Ishii, M., Y. Fukuda, S. Hirahara, S. Yasui, T. Suzuki, and K. Sato, 2017: Accuracy of global upper ocean heat content estimation expected from present observational data sets. *SOLA*, **13**, 163–167, https://doi.org/10.2151/sola.2017-030.

Johnson, G. C., and J. M. Lyman, 2020: Warming trends increasingly dominate global ocean. *Nat. Climate Change*, **10**, 757–761, https://doi.org/10.1038/s41558-020-0822-0.

——, and Coauthors, 2021: Ocean heat content [in "State of the Climate in 2020"]. *Bull. Amer. Meteor. Soc.*, **102** (8), S143–S198, https://doi.org/10.1175/BAMS-D-21-0083.1.

Latif, M., J. Sun, M. Visbeck, and M. Hadi Bordbar, 2022: Natural variability has dominated Atlantic Meridional Overturning Circulation since 1900. *Nat. Climate Change*, **12**, 455–460, https://doi.org/10.1038/s41558-022-01342-4.

Lee, S.-K., W. Park, E. van Sebille, M. O. Baringer, C. Wang, D. B. Enfield, S. G. Yeager, and B. P. Kirtman, 2011: What caused the significant increase in Atlantic Ocean heat content since the mid-20th century? *Geophys. Res. Lett.*, **38**, L17607, https://doi.org/10.1029/2011GL048856.

Levitus, S., and Coauthors, 2012: World ocean heat content and thermosteric sea level change (0–2000 m), 1955–2010. *Geophys. Res. Lett.*, **39**, L10603, https://doi.org/10.1029/2012GL051106.

Li, G., L. Cheng, J. Zhu, K. E. Trenberth, M. E. Mann, and J. P. Abraham, 2020: Increasing ocean stratification over the past half-century. *Nat. Climate Change*, **10**, 1116–1123, https://doi.org/10.1038/s41558-020-00918-2.

Li, L., M. S. Lozier, and F. Li, 2021: Century-long cooling trend in subpolar North Atlantic forced by atmosphere: An alternative explanation. *Climate Dyn.*, **58**, 2249–2267, https://doi.org/10.1007/s00382-021-06003-4.

Li, W., L. Li, M. Ting, and Y. Liu, 2012: Intensification of Northern Hemisphere subtropical highs in a warming climate. *Nat. Geosci.*, **5**, 830–834, https://doi.org/10.1038/ngeo1590.

Li, X., S.-P. Xie, S. T. Gille, and C. Yoo, 2016: Atlantic-induced pan-tropical climate change over the past three decades. *Nat. Climate Change.*, **6**, 275–279, https://doi.org/10.1038/nclimate2840.

Lin, Q.-J., and J.-Y. Yu, 2022: The potential impact of model horizontal resolution on the simulation of atmospheric cloud radiative effect in CMIP6 models. *Terr. Atmos. Oceanic Sci.*, **33**, 21, https://doi.org/10.1007/s44195-022-00021-3.

Liu, W., A. V. Fedorov, S.-P. Xie, and S. Hu, 2020: Climate impacts of a weakened Atlantic Meridional Overturning Circulation in a warming climate. *Nat. Climate Change*, **6**, eaaz4876, https://doi.org/10.1126/sciadv.aaz4876.

Lozier, M. S., S. Leadbetter, R. G. Williams, V. Roussenov, M. S. C. Reed, and N. J. Moore, 2008: The spatial pattern and mechanisms of heat content change in the North Atlantic. *Science*, **319**, 800–803, https://doi.org/10.1126/science.1146436.

Lyman, J. M., and G. C. Johnson, 2014: Estimating global ocean heat content changes in the upper 1800 m since 1950 and the influence of climatology choice. *J. Climate*, **27**, 1945–1957, https://doi.org/10.1175/JCLI-D-12-00752.1.

Lyu, K., X. Zhang, J. A. Church, and Q. Wu, 2020: Processes responsible for the Southern Hemisphere ocean heat uptake and redistribution under anthropogenic warming. *J. Climate*, **33**, 3787–3807, https://doi.org/10.1175/JCLI-D-19-0478.1.

Marshall, J., J. R. Scott, K. C. Armour, J.-M. C. Maxwell, K. C. Anastasia, J. M. Campin, M. Kelley, and A. Romanou, 2015: The ocean's role in the transient response of climate to abrupt greenhouse gas forcing. *Climate Dyn.*, **44**, 2287–2299, https://doi.org/10.1007/s00382-014-2308-0.

Matsumura, Y., and K. I. Ohshima, 2015: Lagrangian modelling of frazil ice in the ocean. *Ann. Glaciol.*, **56**, 373–382, https://doi.org/10.3189/2015AoG69A657.

Ma, X., W. Liu, R. J. Allen, G. Huang, and X. Li, 2020: Dependence of regional ocean heat uptake on anthropogenic warming scenarios. *Sci. Adv.*, **6**, 1–9, https://doi.org/10.1126/sciadv.abc0303.

McCarthy, G. D., and P. W. Thorne, 2018: Sluggish Atlantic circulation could cause global temperatures to surge. *Nature*, **559**, 340–341, https://doi.org/10.1038/d41586-018-05712-x.

McMonigal, K., S. Larson, S. Hu, and R. Kramer, 2023: Historical changes in wind-driven ocean circulation can accelerate global

warming. *Geophys. Res. Lett.*, **50**, e2023GL102846, https://doi.org/10.1029/2023GL102846.

Meehl, G. A., H. Teng, N. Maher, and M. H. England, 2015: Effects of the Mount Pinatubo eruption on decadal climate prediction skill of Pacific sea surface temperatures. *Geophys. Res. Lett.*, **42**, 10 840–10 846, https://doi.org/10.1002/2015GL066608.

Mitas, C. M., and A. Clement, 2005: Has the Hadley cell been strengthening in recent decades? *Geophys. Res. Lett.*, **32**, L03809, https://doi.org/10.1029/2004GL021765.

Myhre, G., and Coauthors, 2013: Anthropogenic and natural radiative forcing. *Climate Change 2013: The Physical Science Basis*, T. F. Stocker et al., Eds., Cambridge University Press, 659–740.

O'Neill, B. C., and Coauthors, 2016: The Scenario Model Intercomparison Project (ScenarioMIP) for CMIP6. *Geosci. Model Dev.*, **9**, 3461–3482, https://doi.org/10.5194/gmd-9-3461-2016.

Palmer, M. D., and K. Haines, 2009: Estimating oceanic heat content change using isotherms. *J. Climate*, **22**, 4953–4969, https://doi.org/10.1175/2009JCLI2823.1.

Park, S., M. A. Alexander, and C. Deser, 2006: The impact of cloud radiative feedback, remote ENSO forcing, and entrainment on the persistence of North Pacific sea surface temperature anomalies. *J. Climate*, **19**, 6243–6261, https://doi.org/10.1175/JCLI3957.1.

Parker, A., and C. Ollier, 2021: The Atlantic meridional overturning circulation is not collapsing. *Quaest. Geogr.*, **40**, 163–167, https://doi.org/10.2478/quageo-2021-0030.

Pikovnik, M., Ž. Zaplotnik, L. Boljka, and N. Žagar, 2022: Metrics of the Hadley circulation strength and associated circulation trends. *Wea. Climate Dyn.*, **3**, 625–644, https://doi.org/10.5194/wcd-3-625-2022.

Power, S., and Coauthors, 2021: Decadal climate variability in the tropical Pacific: Characteristics, causes, predictability, and prospects. *Science*, **374**, eaay9165, https://doi.org/10.1126/science.aay9165.

Rahmstorf, S., J. E. Box, G. Feulner, M. E. Mann, A. Robinson, S. Rutherford, and E. J. Schaffernicht, 2015: Exceptional twentieth-century slowdown in Atlantic Ocean overturning circulation. *Nat. Climate Change*, **5**, 475–480, https://doi.org/10.1038/nclimate2554.

Robson, J., R. Sutton, K. Lohmann, D. Smith, and M. D. Palmer, 2012: Causes of the rapid warming of the North Atlantic Ocean in the mid-1990s. *J. Climate*, **25**, 4116–4134, https://doi.org/10.1175/JCLI-D-11-00443.1.

——, and Coauthors, 2022: The Role of anthropogenic aerosol forcing in the 1850–1985 strengthening of the AMOC in CMIP6 historical simulations. *J. Climate*, **35**, 3243–3263, https://doi.org/10.1175/JCLI-D-22-0124.1.

Romanou, A., J. Marshall, M. Kelley, and J. Scott, 2017: Role of the ocean's AMOC in setting the uptake efficiency of transient tracers. *Geophys. Res. Lett.*, **44**, 5590–5598, https://doi.org/10.1002/2017GL072972.

Rose, B. E. J., K. C. Armour, D. S. Battisti, N. Feldl, and D. D. B. Koll, 2014: The dependence of transient climate sensitivity and radiative feedbacks on the spatial pattern of ocean heat uptake. *Geophys. Res. Lett.*, **41**, 1071–1078, https://doi.org/10.1002/2013GL058955.

Sallenger, A. H., Jr., K. S. Doran, and P. A. Howd, 2012: Hotspot of accelerated sea-level rise on the Atlantic coast of North America. *Nat. Climate Change*, **2**, 884–888, https://doi.org/10.1038/nclimate1597.

Shi, J.-R., S.-P. Xie, and L. D. Talley, 2018: Evolving relative importance of the Southern Ocean and North Atlantic in anthropogenic ocean heat uptake. *J. Climate*, **31**, 7459–7479, https://doi.org/10.1175/JCLI-D-18-0170.1.

——, Y.-O. Kwon, and S. E. Wijffels, 2022: Two distinct modes of climate responses to the anthropogenic aerosol forcing changes. *J. Climate*, **35**, 3445–3457, https://doi.org/10.1175/JCLI-D-21-0656.1.

Shu, Q., Q. Wang, M. Årthun, S. Wang, Z. Song, M. Zhang, and F. Qiao, 2022: Arctic Ocean amplification in a warming climate in CMIP6 models. *Sci. Adv.*, **8**, eabn9755, https://doi.org/10.1126/sciadv.abn9755.

Straneo, F., and P. Heimbach, 2013: North Atlantic warming and the retreat of Greenland's outlet glaciers. *Nature*, **504**, 36–43, https://doi.org/10.1038/nature12854.

Sun, C., J. Li, and F.-F. Jin, 2015: A delayed oscillator model for the quasi-periodic multidecadal variability of the NAO. *Climate Dyn.*, **45**, 2083–2099, https://doi.org/10.1007/s00382-014-2459-z.

——, ——, F. Kucharski, J. Xue, and X. Li, 2019: Contrasting spatial structures of Atlantic Multidecadal Oscillation between observations and slab ocean model simulations. *Climate Dyn.*, **52**, 1395–1411, https://doi.org/10.1007/s00382-018-4201-8.

Sun, X., and R. Wu, 2022: Contribution of wind speed and sea-air humidity difference to the latent heat flux-SST relationship. *Ocean-Land-Atmos. Res.*, **2022**, 9815103, https://doi.org/10.34133/2022/9815103.

Trenberth, K. E., and J. T. Fasullo, 2017: Atlantic meridional heat transports computed from balancing Earth's energy locally. *Geophys. Res. Lett.*, **44**, 1919–1927, https://doi.org/10.1002/2016GL072475.

——, ——, and J. Kiehl, 2009: Earth's global energy budget. *Bull. Amer. Meteor. Soc.*, **90**, 311–324, https://doi.org/10.1175/2008BAMS2634.1.

von Schuckmann, K., and Coauthors, 2016: An imperative to monitor Earth's energy imbalance. *Nat. Climate Change*, **6**, 138–144, https://doi.org/10.1038/nclimate2876.

Wang, C., L. Zhang, S.-K. Lee, L. Wu, and C. R. Mechoso, 2014: A global perspective on CMIP5 climate model biases. *Nat. Climate Change*, **4**, 201–205, https://doi.org/10.1038/nclimate2118.

Wang, G., and Coauthors, 2015: Robust warming pattern of global subtropical oceans and its mechanism. *J. Climate*, **28**, 8574–8584, https://doi.org/10.1175/JCLI-D-14-00809.1.

Wang, Y., J. H. Jiang, and H. Su, 2015: Atmospheric responses to the redistribution of anthropogenic aerosols. *J. Geophys. Res. Atmos.*, **120**, 9625–9641, https://doi.org/10.1002/2015JD023665.

Wernberg, T., and Coauthors, 2016: Climate-driven regime shift of a temperate marine ecosystem. *Science*, **353**, 169–172, https://doi.org/10.1126/science.aad8745.

Worthington, E. L., B. I. Moat, D. A. Smeed, J. V. Mecking, R. Marsh, and G. D. McCarthy, 2021: A 30-year reconstruction of the Atlantic meridional overturning circulation shows no decline. *Ocean Sci.*, **17**, 285–299, https://doi.org/10.5194/os-17-285-2021.

Xie, P., and G. K. Vallis, 2012: The passive and active nature of ocean heat uptake in idealized climate change experiments. *Climate Dyn.*, **38**, 667–684, https://doi.org/10.1007/s00382-011-1063-8.

Yang, H., and Coauthors, 2020: Poleward shift of the major ocean gyres detected in a warming climate. *Geophys. Res. Lett.*, **47**, e2019GL085868, https://doi.org/10.1029/2019GL085868.

——, J. Lu, Q. Wang, X. Shi, and G. Lohmann, 2022: Decoding the dynamics of poleward shifting climate zones using aqua-planet

model simulations. *Climate Dyn.*, **58**, 3513–3526, https://doi.org/10.1007/s00382-021-06112-0.

Zeng, Z., and Coauthors, 2019: A reversal in global terrestrial stilling and its implications for wind energy production. *Nat. Climate Change*, **9**, 979–985, https://doi.org/10.1038/s41558-019-0622-6.

Zhang, R., 2015: Mechanisms for low-frequency variability of summer Arctic sea ice extent. *Proc. Natl. Acad. Sci. USA*, **112**, 4570–4575, https://doi.org/10.1073/pnas.1422296112.

——, S. Sun, Z. Chen, H. Yang, and L. Wu, 2023a: Rapid 21st century weakening of the Agulhas Current in a warming climate. *Geophys. Res. Lett.*, **50**, e2022GL102070, https://doi.org/10.1029/2022GL102070.

——, ——, ——, ——, and ——, 2023b: On the decadal and multi-decadal variability of the Agulhas Current. *J. Phys. Oceanogr.*, **53**, 1011–1024, https://doi.org/10.1175/JPO-D-22-0123.1.

Zhu, C., and Z. Liu, 2020: Weakening Atlantic overturning circulation causes South Atlantic salinity pile-up. *Nat. Climate Change*, **10**, 998–1003, https://doi.org/10.1038/s41558-020-0897-7.

Supplemental Material

Journal of Climate
Substantial Warming of the Atlantic Ocean in CMIP6 Models
https://doi.org/10.1175/JCLI-D-23-0418.1

Supplementary Information

for

Substantial Warming of the Atlantic Ocean in CMIP6 Models

Qiuping Ren[1,*], Young-Oh Kwon[3], Jiayan Yang[3], Rui-Xin

Huang[3], Yuanlong Li[1,2,*], Fan Wang[1,2]

[1]CAS Key Laboratory of Ocean Circulation and Waves, Institute of Oceanology, Chinese Academy of Sciences, Qingdao, China,
[2] Laoshan Laboratory, Qingdao, China,
[3]Woods Hole Oceanographic Institution, Woods Hole, MA, USA,

Supplementary Text:

Some observed and reanalysis data are used to compare with CMIP6 models (Supplementary Fig. 4). Three sea surface temperature (SST) products with 1°×1° horizontal resolutions are analyzed: the monthly Hadley Centre Sea Ice and Sea Surface Temperature dataset (HadISST; Rayner et al. 2003), the Centennial in situ Observation-Based Estimates of the Variability of SST and Marine Meteorological Variables, version-2 (COBE; Hirahara et al. 2014), and the Extended Reconstruction SST, version-5 (ERSST; Huang et al. 2017). For the atmospheric variables (including surface air temperature, total cloud cover, and near-surface zonal wind at 10 m), three atmospheric reanalysis products are used: the 1.875° National Centers for Environmental Prediction–National Center for Atmospheric Research Reanalysis (NCEP; Kalnay et al. 1996), the 2.0° × 1.875° National Oceanic and Atmospheric Administration 20th Century Reanalysis v2 (NOAA20CR; Compo et al. 2011), and the 1° × 1° Japanese 55-year Reanalysis (JRA55; Kobayashi et al. 2015). Long-term change of all variables during 1960-2014 is estimated as the differences between the averages in 1960-1980 and 1994-2014.

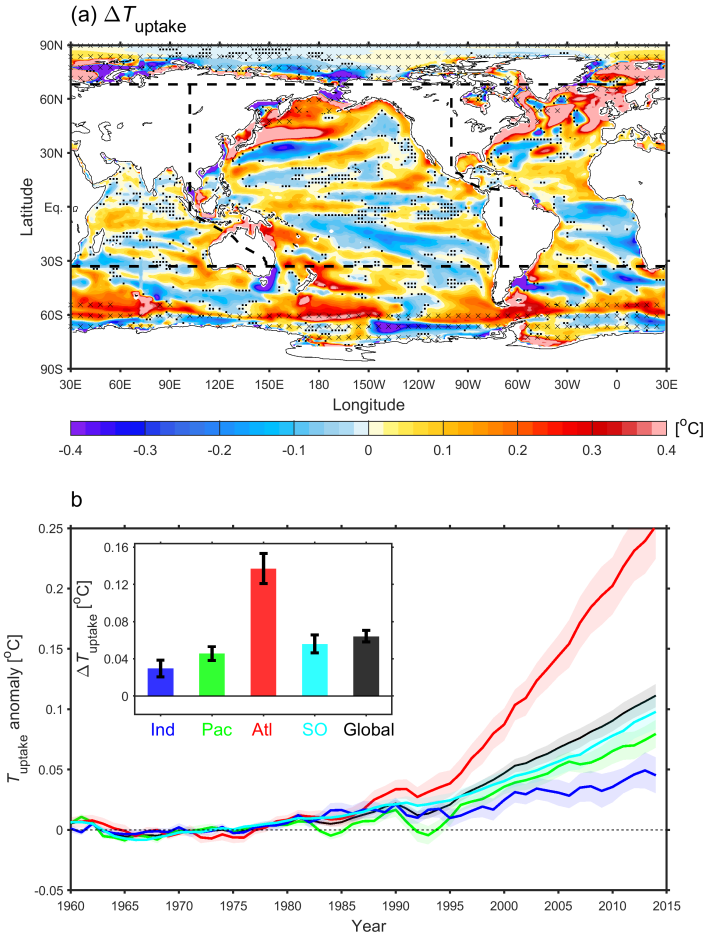

Supplementary FIG. 1. Same as **Figure 3a-b**, but the surface heat uptake in the areas covered by sea ice is computed by combining the surface net heat flux with heat flux into ocean due to frazil ice formation (Q_{net} plus Q_{ice}) for the 10 models with both variables available.

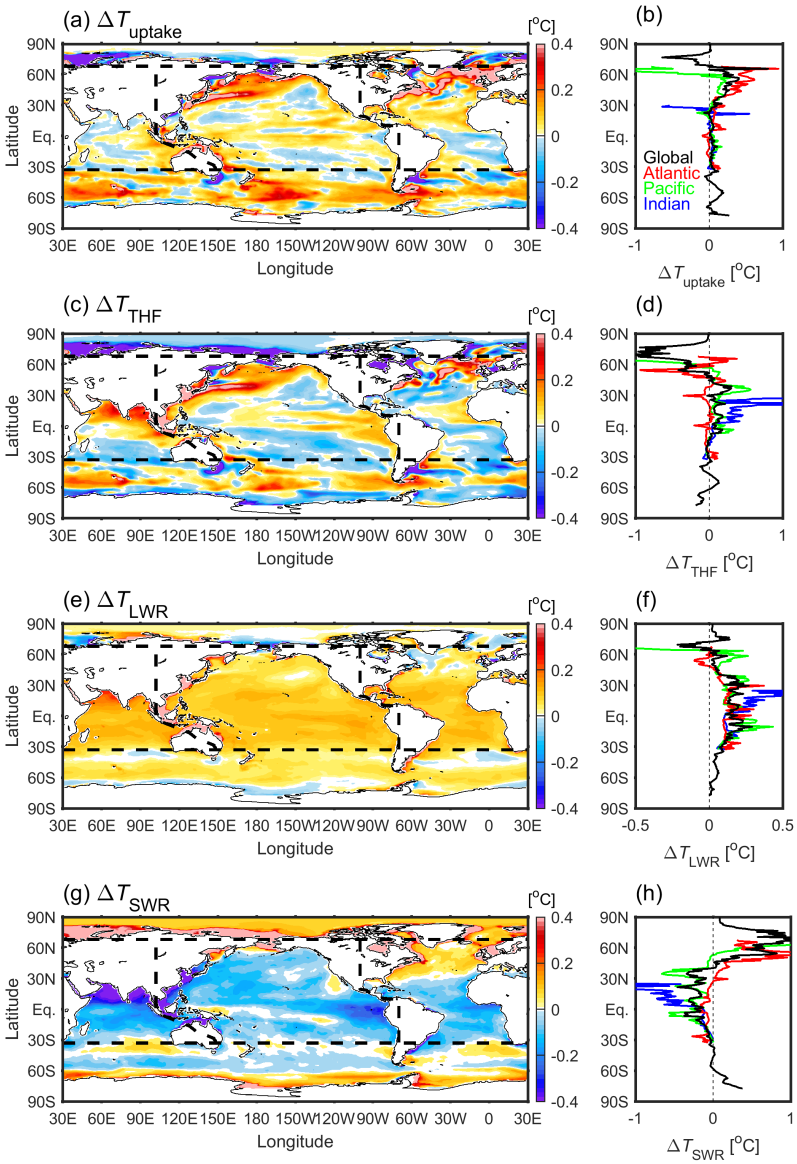

Supplementary FIG. 2. The 0-2000 m temperature changes induced by surface net heat uptake ΔT_{uptake} (a), turbulent heat flux ΔT_{THF} (c), longwave radiation ΔT_{LWR} (e), and shortwave radiation ΔT_{SWR} (g) in the CMIP6 MMM. Zonal-averaged ΔT_{uptake} (b), ΔT_{THF} (d), ΔT_{LWR} (f), and ΔT_{SWR} (h) in the global ocean and individual ocean basins, respectively. All variables are derived from the CMIP6 MMM and shown in unit of ℃. Changes are computed as the differences between the 1994-2014 and 1960-1980 periods.

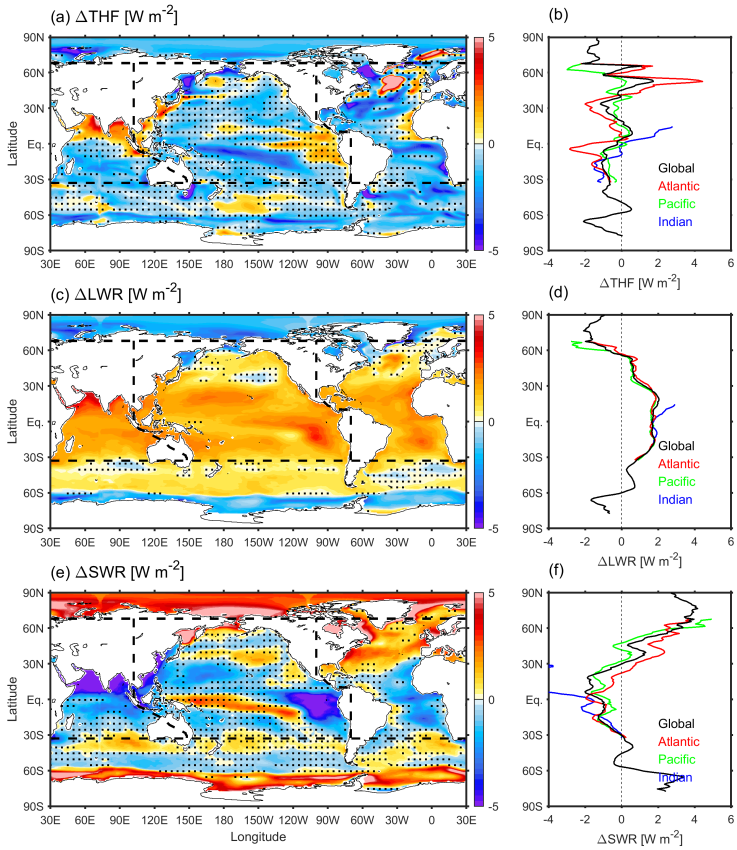

Supplementary FIG. 3. Same as in **Figure. 5c-h**, but using the surface heat fluxes from ocean model outputs of 11 CMIP6 models that provides these surface heat flux components from the ocean models.

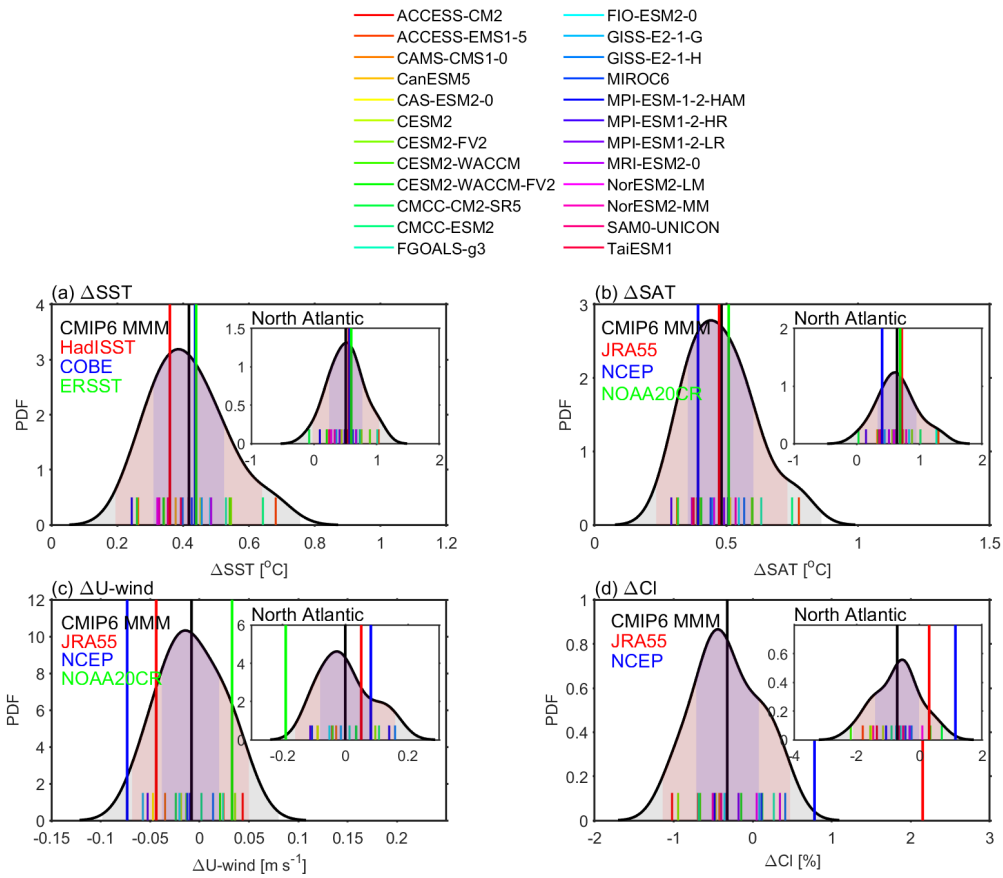

Supplementary FIG. 4. (a) Probability density function (PDF) of basin-averaged ΔSST of the Atlantic Ocean (34°S-68°N) from CMIP6 models. The vertical black line and short colored lines on the horizontal axis mark the ΔSST from the MMM and individual CMIP6 models. Vertical colored lines are ΔSST from the reanalysis datasets. The inset shows the PDF of ΔSST in the subtropical and subpolar North Atlantic Ocean (30°N-68°N). (b)-(d) are the same as (a), but for the PDF of 2-m air temperature change ΔSAT (℃), ΔU-wind at 10 m, and ΔCl. All changes are the differences between the 1994-2014 and 1960-1980 periods.

Supplementary Table. 1. List of CMIP6 model used in this study, along with their global oceanic and atmospheric grid resolutions.

	Institute	Model	Ocean grid (lon×lat)	atmosphere grid (lon×lat)
1	CSIRO-ARCCSS	ACCESS-CM2	360×300	144×192
2	CSIRO	ACCESS-ESM1-5	360×300	145×192
3	CCCma	CanESM5	361×290	128×64
4	CAS	CAS-ESM2-0	360×196	256×128
5	CAMS	CAMS-CMS1-0	360×200	320×160
6	NCAR	CESM2	320×384	288×192
7	NCAR	CESM2-FV2	320×384	144×96
8	NCAR	CESM2-WACCM	320×384	288×192
9	NCAR	CESM2-WACCM-FV2	320×384	144×96
10	CMCC	CMCC-CM2-SR5	362×292	288×192
11	CAS	FGOALS-g3	360×180	180×80
12	FIO-QLNM	FIO-ESM2-0	288×192	288×192
13	NASA-GISS	GISS-E2-1-G	288×180	144×90
14	NASA-GISS	GISS-E2-1-H	360×180	144×90
15	CAS	FGOALS-f3-L	360×180	360×180
16	MIROC	MIROC6	360 × 256	256×128
17	HAMMOZ-Consortium	MPI-ESM-1-2-HAM	256×220	192×96
18	MPI-M	MPI-ESM1-2-HR	802×404	384×192
19	MPI-M	MPI-ESM1-2-LR	256×220	256×220
20	MRI	MRI-ESM2-0	360 × 364	320×160
21	NCC	NorESM2-LM	360×384	144×95
22	NCC	NorESM2-MM	360×384	288×200
23	SNU	SAM0-UNICON	320×384	288×192
24	AS-RCEC	TaiESM1	288×200	288×200

25	THU	CIESM	320×384	320×384
26	EC-Earth-Consortium	EC-Earth3	362×292	512×256
27	EC-Earth-Consortium	EC-Earth3-Veg	362×292	512×256
28	EC-Earth-Consortium	EC-earth3-Veg-LR	362×292	320×160
29	NUIST	NESM3	362×292	192×96

References:

Rayner,N.A., D. E. Parker,E.B. Horton, C. K. Folland, L. V. Alexander, D. P. Rowell, E. C. Kent, and A. Kaplan, 2003: Global analyses of sea surface temperature, sea ice, and night marine air temperature since the late nineteenth century. *J. Geophys. Res*., **108**, 4407, https://doi.org/10.1029/2002JD002670.

Hirahara, S., M. Ishii, and Y. Fukuda, 2014: Centennial-scale sea surface temperature analysis and its uncertainty. *J. Climate*, **27**, 57–75, doi:10.1175/JCLI-D-12-00837.1.

Huang, B., and Coauthors, 2017: Extended Reconstructed Sea Surface Temperature, version 5 (ERSSTV5): Upgrades, vali- dations, and intercomparisons. *J. Climate*, **30**, 8179–8205, https://doi.org/10.1175/JCLI-D-16-0836.1.

Kalnay, E., and Coauthors, 1996: The NCEP/NCAR 40-Year Reanalysis Project. Bull. *Amer. Meteor. Soc.*, **77**, 437–471.

Compo, G. P., and Coauthors, 2011: The Twentieth Century Re- analysis Project. Quart. J. Roy. Meteor. Soc., 137, 1–28, https:// doi.org/10.1002/qj.776.

Kobayashi, S., and Coauthors, 2015: The JRA-55 reanalysis: General specifications and basic characteristics. *J. Meteor. Soc. Japan*, **93**, 5–48, doi:10.2151/jmsj.2015-001.